Gold Solubility in Arc Magmas: Experimental Determination of the Effect of Sulfur at 1000°C and 0.4 GPa

Sébastien Jégo, Michel Pichavant

HAL Id: insu-00671964
https://insu.hal.science/insu-00671964

Submitted on 2 Apr 2012

Gold solubility in arc magmas: Experimental determination of the effect of sulfur at 1000 °C and 0.4 GPa

Sébastien Jégo [ab c]

Michel Pichavant[c]

- [a] Department of Earth Science, Rice University, 6100 Main Street, MS-126, Houston, TX 77005, USA
- [b] Institute of Earth Sciences, Academia Sinica, 128 Academia Road, Sec. 2, Nankang, Taipei 11529, Taiwan, ROC
- [c] Institut des Sciences de la Terre d'Orléans (ISTO) – CNRS: UMR6113 – INSU – Université d'Orléans, France

Abstract

To investigate the behaviour of gold in sulfur-bearing hydrous intermediate calc-alkaline melts under different redox states typical of subduction-zone settings, we have determined the solubility of Au at 0.4 GPa and 1000 °C for three dacitic magmas (two adakites and one calc-alkaline composition) from the North-Luzon Arc (Philippines). The experiments were performed over an oxygen fugacity (fO$_2$) range corresponding to reducing ($\sim$NNO−1), moderately oxidizing ($\sim$NNO+1.5) and strongly oxidizing ($\geqslant$NNO+3) conditions as measured by solid Ni–Pd–O sensors. They were carried out in gold containers, serving also as the source of gold, in presence of variable amounts of H$_2$O and $\sim$1 wt.% of elemental sulfur (S). Concentrations of Au in glasses were determined by laser-ablation inductively-coupled plasma mass spectrometry (LA-ICPMS). Gold solubility in S-bearing melts is drastically enhanced compared to S-free melts, by up to two orders of magnitude. In addition, very high gold solubilities are reached under reducing conditions (<NNO−1) in Fe-poor, S-rich, sulfide-saturated melts probably as a result of an increase of fH$_2$S, and a strong increase of gold solubility is observed at the sulfide/sulfate transition (from $\sim$NNO+1.25 to NNO+1.6) due to the destabilization of sulfides and the increase of melt S^{2-} concentration. Thermodynamic modelling of the experimental results suggest that the dissolution of gold in silicate melt is the result of a combination of various gold species (Au^0, Au$_2$O, Au$_2$O$_3$, Au$_2$S$_3$, Au$_2$(SO$_4$)$_3$, and Au$_2$FeS$_2$) present in the melt in variable proportions, depending on the three parameters considered in the model – log fO$_2$, log fS$_2$ and log X_{FeS} – which are the main variables controlling the dissolution of gold in melt under our experimental PTX conditions. Our modelling shows that Au$_2$FeS$_2$ is the main gold species dissolved under reducing conditions (i.e., S^{6+}/S$_{total}$ $\sim$ 0), whereas at sulfate saturation gold is mainly dissolved as Au metal and Au$_2$O. The present study shows that sulfide undersaturation of primary mantle magmas or/and highly oxidizing conditions are not required for metal mobilization from the source, since gold enrichment in evolving arc magmas and exsolving fluid phases is likely to occur over a wide range of fO$_2$ at sulfide saturation, from ΔNNO<−1 to the sulfide–sulfate transition (i.e., NNO+0.5–2.0); nevertheless it is critically controlled by variations of fS$_2$ and fH$_2$S. The role of Au-enriched slab partial melts and slab-derived aqueous fluids, and the importance of the abundance of sulfur in the source for an early gold enrichment in the melt, are emphasized.

1. Introduction

On a worldwide scale, Au–Ag–Cu–Mo epithermal and porphyry-type deposits are spatially and temporally associated with intrusive arc magmatism ([Sillitoe, 1989], [Sillitoe and Bonham, 1990], [Sillitoe, 1997], [Ulrich et al., 1999] and [Halter et al., 2002]), and it is generally accepted that such deposits result from a combination of magmatic and hydrothermal processes ([White and Hedenquist, 1990], [Hedenquist and Lowenstern, 1994] and [White and Hedenquist, 1995]). Magma bodies may chemically contribute to the mineralizing systems by supplying elements which, upon volatile exsolution, are transferred into the magmatic-hydrothermal fluid phase. However, the origin of metals (Au, Ag, Cu, Mo) in epithermal and porphyry-type deposits has long been a subject of debate, with metallogenic models dividing in essentially two groups, one group suggesting that metals originate in country rocks (e.g., [Keays and Skinner, 1989] and [Mathur et al., 2000]), and a second group of models considering that magmatic intrusions constitute the source of metals. These can be pre-concentrated through igneous differentiation processes, before being transferred to the magmatic-hydrothermal fluid phase ([Ulrich et al., 1999], [Halter et al., 2002] and [Harris et al., 2003]). Certain components of hydrothermal fluids such as halogens and sulfur originate from magmatic sources (Hattori and Keith, 2001). The observation that primary ore minerals are predominantly sulfides (e.g., Kesler et al., 2002) has led to the suggestion that sulfur may play an important role in metal enrichment processes at the magmatic stage ([Sillitoe, 1997] and [Mungall, 2002a]). More specifically in the Philippines, [Imai, 2002] and [Imai, 2004] reports that sulfur is systematically present in all Au–Cu deposits of the North Luzon arc, either as sulfide minerals (chalcopyrite, pyrite, bornite, pyrrhotite) or as sulfate (anhydrite) – reflecting an evolution of the redox state within single deposits.

Previously, the solubility of noble metals, including gold, was studied in basaltic liquids saturated with sulfides (ΔFMQ < -1) and sulfates (ΔFMQ $\geqslant +1.9$) at 1300 °C and 1 GPa (Jugo et al., 2005a), although these data were not given in detail. Several other experimental studies have focused on the quantitative evaluation of Au partitioning between Au metal, rhyolitic or basaltic melts, coexisting fluids (vapour/brine) and sulfides (crystal/melt) in S-bearing magmatic assemblages ([Bezmen et al., 1994], [Fleet et al., 1996], [Fleet et al., 1999], [Crocket et al., 1997], [Jana and Walker, 1997], [Jugo et al., 1999], [Simon et al., 2007], [Simon et al., 2008] and [Bell et al., 2009]). Recently, Botcharnikov et al. (2010) presented the first experimental Au solubility data in S-bearing hydrous intermediate (i.e., andesitic) silicate melts at 1050 °C and 0.2 GPa under fO$_2$ close to the Ni–NiO (NNO) buffer. However, none of those studies considered the effect of a variable oxidation state on the behaviour of gold in sulfur-saturated melts. In contrast, Jégo et al. (2010) investigated the dissolution mechanism of gold in S-free hydrous intermediate (i.e., dacitic) silicate melts at 1000 °C and 0.4 GPa over a wide fO$_2$ range (from ∼NNO−1.5 to ∼NNO+2.6), and showed that the addition of sulfur under reducing conditions (∼NNO−1) dramatically enhanced the solubility of gold (by a factor of 25–85) in comparison with S-free melts at the same fO$_2$. Their data, together with those of Botcharnikov et al. (2010), suggest a positive correlation between the concentrations of Au and S dissolved in the melt under reducing conditions (i.e., sulfur occurring mainly as S^{2-} species). In addition, Botcharnikov et al. (2011) explored the effect of variable redox conditions (from FMQ−0.4 to FMQ+3.3) on gold solubility in hydrous basaltic and andesitic melts at 1050 °C and 0.2 GPa, and found that Au solubility in silicate melts is highest within a narrow window of fO$_2$ characterized by the transformation of sulfide to sulfate species in the magma.

In this study, we use an experimental approach to explore the hypothesis that S-bearing magmas have the ability to pre-concentrate Au at the magmatic stage and, therefore, represent Au-enriched magmas over a wide range of fO$_2$. A comprehensive experimental dataset is provided that allows to clarify the influence of S and its interplay with the effect of fO$_2$ on the solubility of gold in dacitic silicate melts. The experimental results allow the transport properties for Au in S-free and S-bearing magmas to be compared. They also place constraints on mechanisms of Au complexation in hydrous magmatic liquids of dacitic composition, typical of arc settings. The critical importance of both fO$_2$ and fS$_2$ on Au transport in S-bearing magmas is emphasized.

2. Starting materials and experimental strategy

2.1. Starting materials

Our experiments were performed in parallel on three natural samples, all from the North Luzon arc (Philippines), respectively representative of a typical adakite (Bal2), an intermediate adakite (Pin Dac) and a typical calc-alkaline magma (PhM5) after the definition of Jégo et al. (2005) (a summary of this adakite classification is given in Jégo et al. (2010)). Recent (<20 Ma) magmatism in the North Luzon arc is linked to the current subduction of the South China Sea plate along the Manila Trench, and produces a range of arc rocks ([Sajona and Maury, 1998], [Prouteau et al., 2000], [Yumul et al., 2000], [Bellon and Yumul, 2001] and [Jégo et al., 2005]). World-class Cu–Au deposits are spatially and temporally associated with this recent magmatic activity, as shown by the chain of porphyry copper deposits extending from Dizon in the south to Lepanto in the north, and the epithermal Au deposits of the Baguio district ([Bellon and Yumul, 2000], [Imai, 2001] and [Imai, 2002]). In the Baguio district, there is an intimate association between intrusive rocks and mineralization (Santo Tomas II Cu–Au porphyry and Antamok and Acupan epithermal Au deposits, [Imai, 2001], [Imai, 2002] and [Polvé et al., 2007]). The three starting rocks selected are all samples of this recent magmatic episode in North Luzon. Their respective sampling location and geochemical characteristics (major and trace elements) are described in detail by Jégo et al. (2010). It is worth stressing here, though, that the three starting samples have intermediate SiO$_2$ contents, within a narrow range (63.4–65.1 wt.%, Table 1).

Sulfur contents in starting materials (double-melting glass) are below the detection limits of the electron-probe micro-analysis (EPMA) apparatus (Table 1; Section 3.4.1), i.e., less than 30 ppm. Besides the fact that we avoided starting samples containing anhydrite crystals, such low S contents are likely be due to volatilization and loss of sulfur during the preparation by double melting of the starting rock glass powder at 1400 °C in air. The bulk gold contents of our samples are quite low (12–38 ppb; Table 1), close to the detection limit (⩽10 ppb for ICP-MS, Toulouse, France); these Au concentrations are in the same range as those measured by Borisova et al. (2006) in the rhyolitic matrix glass of the Pinatubo 1991 white dacite (22 ± 8 ppb). Note that the typical adakite Bal2 is the most Au-enriched.

2.2. Experimental strategy

The aim of this study is to investigate the effect of both sulfur and fO$_2$ on the solubility of Au in hydrous intermediate silicate melts, in order to quantitatively evaluate their transport properties for gold at the magmatic stage (i.e., as opposed to the hydrothermal stage). The experiments complement and extend the study of Jégo et al. (2010) since they have been

performed on the same starting materials and in the same conditions of pressure and temperature.

To simulate conditions of evolution of intermediate arc melts as closely as possible in the experiments, a pressure of 0.4 GPa was chosen, and an elevated temperature (1000 °C), close to the liquidus of dacitic compositions such as the three starting rocks (e.g., Prouteau and Scaillet, 2003), was adopted. Hydrous conditions were imposed, the run temperature and pressure allowing the concentration of H_2O in melt to be varied without inducing significant crystallization of silicate phases. The experimental fO_2 was varied from relatively reducing (~NNO−1), moderately oxidizing (~NNO+1.5) to highly oxidizing (NNO ⩾ 3) conditions, in a range encompassing the fO_2 of most of natural arc magmas. In order to explore the effect of sulfur saturation on Au solubility, all experiments reported in this study were performed with addition of elemental S.

3. Experimental and analytical methods

3.1. Experimental charges

Each of the three natural samples was ground in an agate mortar, then placed in a Pt crucible and fused at 1400 °C, 1 atm, in air for 4 h. Two cycles of melting were performed to produce chemically homogeneous glasses which were then crushed. About 30 mg of glass powder was loaded into pure gold capsules (2.5 mm ID, 2.9 mm OD, 15 mm length) after homogeneous mixing with ~1 wt.% of pure elemental sulfur (S), together with variable amounts of deionized water (between 5 and 10 wt.% of the total charge), depending on the desired melt water content. The experimental capsules were welded shut with a graphite arc-welder, and then stored in an oven at 110 °C to ensure homogeneous water distribution and also to check for leaks.

In this study, the source of Au was the container capsule. Au is relatively inert with respect to Fe-bearing charges. The equilibration of charges with respect to the imposed fH_2 is limited by the in-diffusion of H_2 through the capsule and by the redox reactions inside the capsule. Au is known experimentally to be quite permeable to H_2 at elevated temperatures (e.g., [Chou, 1986], [Gunter et al., 1987], [Linnen et al., 1995] and [Truckenbrodt and Johannes, 1999]; see also Jégo et al., 2010). For our experimental conditions (in particular temperature and Au capsule wall thickness), charges equilibrate with the fH_2 imposed inside the pressure vessel in timescales of the order of 10 min ([Scaillet et al., 1992] and [Schmidt et al., 1997]). This is much less than our experimental durations (~100 h), and it shows that redox control was effectively achieved in our experiments (Jégo et al., 2010).

3.2. Oxygen fugacity sensors

Experimental redox conditions were determined by the solid sensor technique ([Taylor et al., 1992] and [Pownceby and O'Neill, 1994]). The sensor assemblage consisted of a mixture of metal M + Pd metal powders in variable proportions, plus metal oxide (MO). For experiments above the NNO buffer, Ni–Pd metallic alloys + NiO metal-oxide were used (i.e., M = Ni), and for experiments below NNO buffer, Co–Pd + CoO mixtures (M = Co). For each experiment, two pellets of the appropriate sensor assemblage were prepared, with a high and low M/Pd ratio, respectively. These were loaded into a 20 mm length Pt capsule containing ~10 mg of deionized water, lined with ZrO_2 powder to prevent alloying between the pellets and the capsule walls. The sensor Pt capsule was welded shut and stored for 24 h in an oven at 110 °C

to check for leaks, before being placed together with the experimental Au capsules inside a thin alumina tube sample holder.

3.3. Experimental equipment and procedure

All experiments were performed at 400 MPa and 1000 °C in a vertical internally heated pressure vessel (IHPV). Either a molybdenum or kanthal double-resistance furnace was used, allowing the 4–6 cm hot spot zone to be focused at the level of the sample holder, with a thermal gradient less than 2 °C across (Roux and Lefèvre, 1992). Temperature was measured by two sheathed chromel–alumel thermocouples, calibrated at 1 atm against the melting point of NaCl (800.5 °C), and is considered known to within ±5 °C. Total pressure was monitored by a factory-calibrated Heise gauge, accurate to within 20 bars. Redox conditions were imposed and controlled by the fH$_2$ prevailing in the pressure vessel. The IHPV was pressurized with either pure Ar gas or a mixture of Ar and H$_2$ gases. In the case of pure Ar pressure medium, the intrinsic fH$_2$ of the vessel is extremely low and imposes a very high fO$_2$ (log fO$_2$ ∼ NNO+3.4) when calculated under water-saturated conditions (i.e., aH$_2$O = 1). To impose more reducing experimental conditions, Ar–H$_2$ mixtures generated by sequential loading of H$_2$ and Ar were used (see Scaillet et al. (1995) for additional details). Experimental redox conditions corresponding to log fO$_2$ of the order of NNO+1 and NNO−1 were obtained by loading respectively about 1.5 bar and 15 bars of H$_2$ gas in the vessel before Ar pressurization and heating (i.e., at ambient P and T). The fH$_2$ values reported in Table 2 correspond to values calculated from the fO$_2$ of the sensors, i.e., to the experimental fH$_2$. The experiments were rapidly quenched by electrically melting the Pt wire that suspended the sample holder in the vessel hot spot zone (Roux and Lefèvre, 1992; Di Carlo et al., 2006). This caused the sample holder to drop to the cold end of the vessel with quench rate of the order of 300 °C/s (Roux and Lefèvre, 1992). The duration of the runs was generally between 100 and 120 h. We show below that such durations are sufficient to produce experimental glasses with homogeneous Au concentrations believed to represent equilibrium values.

3.4. Analytical methods

After each experiment, the capsules were checked for leaks by weighing, then opened, and the experimental products were prepared for analysis.

3.4.1. Major and minor elements

Glass fragments were mounted in epoxy, polished successively to a final diamond grit of 1 μm, and coated with a ∼0.03 μm carbon film by using a standard thermal evaporation technique. Experimental glasses were analyzed for major elements with a Cameca SX50 electron microprobe (BRGM-CNRS facility, Orléans) equipped with five spectrometers. All data were obtained using 15 kV acceleration voltage, 6 nA beam current, a defocused electron beam (10 μm diameter) and peak counting times of 10 s. Multiple measurements were made for each sample (∼10 spot analyses) to increase analytical accuracy and check for the chemical homogeneity of the glasses. Natural reference minerals were used as standards. To minimize the effect of migration of the alkalis (Na, K) under the beam in hydrous glasses, the alkali concentrations measured in the glass were adjusted by applying a correction factor, function of the glass H$_2$O content, determined as follows: the Na$_2$O and K$_2$O concentrations measured in the hydrous experimental glasses of a given starting composition (i.e., Bal2, Pin Dac or PhM5) and acquired during the same electron microprobe analytical session (to minimize the time-dependent instrumental drift) were plotted in a diagram [Na$_2$O]$_{glass}$ or

[K$_2$O]$_{glass}$ normalized to 100 wt.% vs. [H$_2$O]$_{glass}$ (*cf*. Section 3.4.2 for the determination of [H$_2$O]$_{glass}$), together with the [Na$_2$O]$_{glass}$ or [K$_2$O]$_{glass}$ of the corresponding anhydrous starting composition taken as secondary reference for [H$_2$O]$_{glass}$ = 0; in such a diagram, the data describe a well defined straight line with a negative slope, the absolute value of this slope representing the Na$_2$O or K$_2$O correction factor for hydrous glasses of a given starting composition and for a given analytical session. The [H$_2$O]$_{glass}$ of a given charge is then multiplied by the corresponding correction factor, and the product is added to the non-normalized value of the [Na$_2$O]$_{glass}$ or [K$_2$O]$_{glass}$ of the charge; the result represents the corrected glass Na$_2$O or K$_2$O content of the charge.

The composition of silicate mineral phases present in some experimental charges (mostly clinopyroxene) was determined as above (15 kV acceleration voltage, 6 nA beam current, peak counting times of 10 s) and using a focused electron beam (~1 μm diameter). The major element composition of oxide (magnetite) and sulfide (pyrrhotite) mineral phases was determined using 15 kV acceleration voltage, 20 nA beam current, a focused electron beam (~1 μm diameter) and peak counting times of 10 s. Hematite, pyrrhotite, anhydrite and pure metals were used as standards. We also intended to detect Au as a minor component in those oxides and sulfides. A counting time of 30 s and a beam current as high as 250 nA were used to reduce the limit of detection for Au. However, although a detection limit as low as 330 ppm (calculations after Ancey et al. (1978)) was obtained, no trace of Au was found. Attempts were also made to analyze the Au-nuggets (see below) despite their tiny size; the results confirmed that Au is the main component of these particles.

Sulfur in the starting glasses was measured by electron microprobe (JEOL JXA-8500F) in Taipei, Taiwan (IES-AS facility). Sulfur contents were always found to be below the detection limit (Table 1), even when using 15 kV acceleration voltage, 50 nA beam current, a defocused electron beam (10 μm diameter) and peak counting times as long as 500 s. Such analytical parameters lower the limit of detection to less than 30 ppm S (calculated as three times the standard deviation of replicate measurements). Pyrite was used for calibration.

Sulfur in experimental glasses was analyzed with a Cameca Camebax electron microprobe (BRGM-CNRS facility, Orléans) equipped with four spectrometers. This equipment, contrary to the SX50 probe, allows us to determine the concentration of a given element with each of the four spectrometers, simultaneously, leading to more accurate results. The data were obtained using 15 kV acceleration voltage, 50 nA beam current, a defocused electron beam (10 μm diameter) and peak counting times of 10 s. The detection limit corresponding to such analytical parameters is of the order of 80 ppm S (Clemente et al., 2004). The reduced to moderately oxidized experimental charges (runs No. 1, 3, 5 and 6; NNO−1 < log fO$_2$ < NNO+2; see Table 2 and Fig. 1) contain only sulfides (pyrrhotite). However, depending on the P–T–fO$_2$–fS$_2$ conditions and the silicate melt composition, saturation with a solid sulfide does not imply absence of an oxidized S species dissolved in the melt. Therefore, since the position of the Kα line is dependent on the valency of sulfur, both peaks corresponding to S^{2-} and S^{6+} species were checked in those charges. The proportion of sulfur occurring as S^{6+} species appeared to be negligible, and so only the position corresponding to S^{2-} was chosen for analysing the reduced and moderately oxidized charges. In contrast, the run No. 4 conducted under highly oxidizing conditions (fO$_2$ > NNO+3) contains sulfate (anhydrite) associated with magnetite at equilibrium, and the Kα position corresponding to S^{6+} was chosen for this charge. Three dacitic standard glasses were used for calibration, with respective sulfur contents of 750, 1400 and 1900 ppm S. The

analysis of these glass standards during each analytical session allowed calibration of the sulfur concentration as a function of the measured X-ray counts.

The Cameca Camebax electron microprobe was also used for determining the composition of the solid sensors. The metals analyzed were Ni, Co and Pd, together with Pt, Fe and S to check for contamination from the capsule. The data were obtained using 15 kV acceleration voltage, 21.5 nA beam current, a defocused electron beam (10 μm diameter) and peak counting times of 10 s. Pyrrhotite and pure metals were used for calibration.

3.4.2. H_2O concentrations in experimental glasses

H_2O contents of experimental glasses were determined by a Karl–Fischer coulometric titration method (Westrich, 1987). The apparatus employed was a Mettler Toledo KF DL 32 coulometer. For each experimental charge, multiple (at least three) measurements were made successively; the average of these multiple measurements and the corresponding standard deviation ($\pm 1\sigma$) are reported in Table 2. For each measurement, a 5–10 mg fragment of silicate glass was placed in a Pt crucible before being melted at 1300 °C in 5 min in an induction furnace. The amount of water vapour released from the silicate melt was then measured in the titration cell of the coulometer. The analytical error of this method, even for very low water contents, is less than 0.1 wt.%, but a residual amount of ~0.1 wt.% H_2O has been shown to remain in the molten glass at 1100 °C ([Westrich, 1987], [Holtz et al., 1992], [Holtz et al., 1995], [Behrens, 1995] and [Behrens et al., 1996]). Therefore, a correction was applied to the raw data by systematically adding 0.1 wt.% H_2O to the measured water concentration for all charges. For crystal-bearing charges, the glass H_2O concentration was calculated from the corrected value by subtracting the amount of crystals present, estimated by mass balance (see below).

3.4.3. Gold concentrations

Gold contents in experimental glasses were determined using laser ablation ICP-MS system at the Research School of Earth Sciences (RSES) of the Australian National University (ANU, Canberra). This system consists of a Lambda Physik LPX 1201 pulsed ArF excimer laser coupled to a Agilent 7500 ICP-MS (Sun et al., 2004). NIST 612 was used as the external standard, and the isotope 29 of Si (^{29}Si) was used as an internal standard with Si being calibrated against concentrations measured by EPMA.

Each signal (*cf*. Fig. 2a) consists of a first part corresponding to background (laser off) and a second part corresponding to the actual measurement (laser on). The ablation was performed by laser drilling; thus the hole drilled becomes progressively deeper with time. The data were obtained using 22 kV acceleration potential, 120 mJ energy and a variable laser power from 0.6 to 1.3 W. The diameter of the laser beam and the pulsation frequency were optimized to 40 μm and 5 Hz, respectively, during 60 s, leading to a 20–25 μm deep hole. A background time of half the ablation time (i.e., 20 or 30 s) was chosen. At least three analyses were made for each experimental charge to check for homogeneity. The NIST 612 standard (Au = 4.58 ppm; Sun et al., 2004) was used for calibration and the calculation of Au concentrations. Besides gold and other noble metals, tantalum (Ta) was analyzed because this element may interfere with Au, following:

$$^{181}Ta + {}^{16}O \Leftrightarrow {}^{197}Au$$
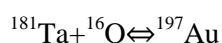
This interference was corrected for based on the Ta concentrations; nevertheless, the difference between uncorrected and corrected results ranges from −1% (some uncorrected values lying slightly below the corresponding corrected concentration) to 10%, within the analytical errors (see supplementary information in Sun et al. (2004)).

The detection limit (DL) for Au are shown in Table 2 for each experimental charge. Each analytical point of every charge has its own DL, although all analyses were conducted with the same laser beam diameter (40 μm). Here, the detection limits were calculated as three times the standard deviation of three replicate measurements of the background noise (representative of the analytical blank). Therefore, for a given analytical point, DL may vary inversely with the duration of the flat (i.e., spike-free) part of the ablation signal used for the calculation of Au concentrations (*cf*. Fig. 2), relative to both standards and background. However, DL are always significantly lower than measured glass gold concentrations. The highest DL/[Au] ratio ([Au] being the gold concentration in glass) of our dataset is about 0.74 for one analytical point in charge C5A. Nevertheless, most charges have very low DL/[Au], in the range 2.10^{-4} to <0.07. Only the highly oxidized run (No. 4) shows higher ratios (max. 0.25–0.59 depending on the charge) resulting from both lower Au melt contents and higher DL values (due to a larger proportion of Au-nuggets in those charges than in more reduced ones). Moreover, the σ/[Au] values (σ being the statistic standard deviation of n replicate measurements of glass gold content in one charge) are generally low, most of the experimental charges showing σ/[Au] values lower than or equal to 0.10. This demonstrates the high sensitivity of our gold concentration measurements and strongly suggests that gold is homogeneously distributed in our experimental glasses, a condition necessary for the attainment of equilibrium in the experiments. In run No. 4, though, σ/[Au] ratios show higher values – up to 0.44 (charge C6D) – due to the abundance of Au-nuggets disseminated in the very oxidized melts, as shown in Fig. 2b, which adversely affect the LA-ICP-MS signal, and thus increase significantly the DL.

3.4.4. Analytical data processing

For each charge, water activity (aH$_2$O) was calculated from the H$_2$O content and the major element (excluding S) composition of glass, using the model of Burnham (1979). Oxygen fugacity (fO$_2$, referenced to the NNO equilibrium at 0.4 GPa standard pressure and 1000 °C standard temperature, Pownceby and O'Neill, 1994) was calculated from both experimental fH$_2$ and fH$_2$O (the latter obtained from aH$_2$O), following the water dissociation equilibrium:

$$f\mathrm{O}_2 = (K_\mathrm{W} \cdot f\mathrm{H}_2\mathrm{O}/f\mathrm{H}_2)^2$$

with K_w taken from Robie et al. (1978). Experimental fH$_2$ was determined from the sensor capsule since fO$_2$ is known from the composition of the alloy phase ([Taylor et al., 1992] and [Pownceby and O'Neill, 1994]) and H$_2$O is present in excess (hence fH$_2$O = fH$_2$O°). The fO$_2$ is known to better than 0.25 log units ([Scaillet et al., 1995] and [Martel et al., 1999]).

The fS$_2$ in reduced/moderately oxidized charges was calculated at 0.4 GPa/1000 °C from the composition of pyrrhotite (i.e., X_{FeS}; Froese and Gunter, 1976). The accuracy of the pyrrhotite analyses (see Table 5) allows this method of calculation to be used with our data.

The fS$_2$ in highly oxidized charges was determined from mineral–melt equilibria involving the anhydrite + magnetite assemblage (*cf*. Appendix A.1).

The fSO$_2$ and fH$_2$S were obtained by assuming ideal mixing between all volatile species at equilibrium at the experimental pressure and temperature (i.e., 0.4 GPa/1000 °C). They were calculated from the following equilibrium reactions:

$$\frac{1}{2}S_2 + O_2 = SO_2$$

$$H_2O + \frac{1}{2}S_2 = H_2S + \frac{1}{2}O_2$$
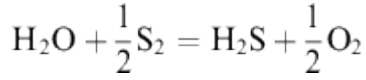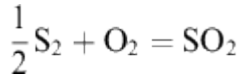
Thus, with the corresponding equilibrium constants K, it comes:

$$f SO_2 = K_3 \cdot f O_2 \cdot f S_2^{1/2}$$

$$f H_2S = (K_4 \cdot f H_2O \cdot f S_2^{1/2})/f O_2^{1/2}$$

Values of fO$_2$, fS$_2$ and fH$_2$O are known at 0.4 GPa standard pressure, and the equilibrium constants K_3 and K_4 are expressed as a function of the experimental temperature T (in K), according to Ohmoto and Kerrick (1977):

$\log K_1 = (18929/T) - 3.783$

$\log K_2 = (-8117/T) + (0.188 \log T) - 0.352$

The crystallinity of experimental charges was determined by mass balance, using the electron microprobe compositions of the starting glass and of all condensed phases present. The calculations were performed using a least-squares technique adapted from Albarède (1995) based on 8 major oxides, excluding MnO and H$_2$O, the total being constrained to unity. Phase proportions were calculated together with model bulk composition.

4. Results

Results for a total of 38 S-doped charges (including six S-doped charges already presented in Jégo et al., 2010: C1E-C3E, C1F-C3F) are reported together with experimental conditions in Table 2.

4.1. Intensive variables (aH$_2$O, fO$_2$, fS$_2$)

H$_2$O contents in glass range from 3.44 to 8.03 wt.% (Table 2), with corresponding aH$_2$O values ranging from 0.36 to saturation (i.e., aH$_2$O = 1), the latter condition being attained in one charge only (C1F). The H$_2$O concentration in Pin Dac melt at saturation is close to 8 wt.% (as shown by charges C1E and C1F, both at 8.03 wt.%). It differs little from the two other investigated melts, owing to their similar major element compositions (C4F (Bal2): aH$_2$O = 0.97 at 7.72 wt.% H$_2$O; C8E (PhM5): aH$_2$O = 0.95 at 7.94 wt.% H$_2$O). Some H$_2$O-rich charges reported in Table 2 (e.g., C1E, C1F, C3F) have uncertainties (i.e., standard deviation of multiple H$_2$O measurements) of about 1 wt.%, suggesting that water is less homogeneously distributed in these glasses than in the other charges; it is actually most probably due to the presence of trapped fluids (i.e., tiny bubbles) in those fluid-saturated

glasses, which may have led to slightly different bulk H_2O contents after multiple measurements by KFT titration.

Oxygen fugacity values range from NNO−1.19 to NNO+3.55 (Table 2). A wide fO_2 range has thus been investigated, encompassing different redox conditions (Fig. 1; see Appendix A.2 for the calculation of stability fields): reducing (runs 5 and 6), moderately oxidizing (runs 1 and 3) and highly oxidizing (run 4). The calculated fS_2 values vary by almost seven orders of magnitude ($-3.76 < \log fS_2 < 3.16$), while melt sulfur concentrations range from 256 to 2422 ppm.

4.2. Experimental products and compositions

All experimental charges mostly comprise silicate glass, and some of them contain a small proportion (<5 wt.%) of crystalline phases (silicates, sulfides, oxides, sulfates, metallic phases, Table 2; see Fig. 3 for textures typical of most of our run products), in accordance with the (sub-)liquidus experimental conditions. Due to the relatively low solubility of S in silicate melts, which systematically induces the formation of a S-rich fluid phase at equilibrium (mainly composed of $H_2S + SO_2 + S_2 + H_2O$), a vapour phase is considered to be systematically present (i.e., the system is fluid-saturated), even if the melt is strictly-speaking H_2O-undersaturated ($aH_2O < 1$) under the experimental conditions (see Section 3.4.4). Then, the presence of a vapour phase leads to significant partitioning of all components from silicate melt to vapour, notably gold (e.g., [Ulrich et al., 1999], [Sun et al., 2004] and [Simon et al., 2007]). Given the amounts of H_2O initially loaded into the capsules, this vapour phase is present in very low amounts (<2–3 wt.% of the total charge). Additionally, most of the exsolved fluid phase is external to the glass bead, i.e., it is not trapped as bubbles or fluid inclusions. Therefore, gold concentrations obtained by ablating the glass are believed to truly reflect those in the melt, and not the combined melt + fluid gold contents. We did not examine here the partitioning of gold between melt and fluid since the main goal of the present study was to examine the effect of sulfur on the solubility and transport of gold in melt at the magmatic stage. Gold partitioning between fluid and melt has been investigated in a few previous studies ([Frank et al., 2002], [Simon et al., 2005] and [Simon et al., 2007]).

Diopside-rich clinopyroxene (cpx; Table 3), mostly less than 20 μm in size (Fig. 3a), appears as the silicate liquidus phase in several experiments. Nevertheless many charges from this study are silicate crystal-free. None of the PhM5 charges crystallized any silicate phase, suggesting a slightly lower liquidus temperature for this composition than for the two others. Enstatite-rich orthopyroxene (opx) occurs in small amounts in charge C6D, and constitutes the only silicate phase crystallized in run 4 (Table 2). The very oxidizing conditions of this experiment are certainly responsible for the crystallization of opx, due to the fractionation of calcium by anhydrite ($CaSO_4$) crystallization and to the availability of iron because of sulfide instability. Oxides are found only in the most oxidizing experiment (run 4), often texturally associated with anhydrite; most have a size from <1 to a few μm (Fig. 3b and c). Satisfactory electron microprobe analyses were obtained for oxides from charges C3D and C7D–C9D (Table 4) and showed that these oxide phases are magnetites (mgt). Sulfides are present in every charge of the reduced/moderately oxidizing runs (Fig. 3a). They all have similar Fe/S atomic ratios, close to 1, implying that these sulfides are pyrrhotites ($Fe_{1-x}S$, with $0 < x < 0.2$; see Table 5). No evidence was found (from the composition of sulfides) for the presence of an immiscible Fe–S–O sulfide liquid under our experimental conditions. About 2 wt.% of sulfate mineral phases (anhydrite) are found in every assemblage of the most oxidizing experiment (Table 2), commonly associated to mgt and Au–nuggets (Fig. 3c). Samples run at moderately oxidizing conditions

(~NNO+1.5) contain sulfide phases. However, as shown in Fig. 1, these moderately oxidized charges plot very close to the anhydrite stability field.

Major element compositions of experimental glasses are given in Table 6. They are quite similar to their respective starting glass compositions, since the proportion of condensed phases is always very small in the run products and there was no substantial partitioning of major elements to the fluid phase. However significant depletions in FeO and/or CaO, and to a lesser extent in MgO, associated with slight enrichments in Na_2O and Al_2O_3 occur in most glasses when compared to the respective starting compositions, but still in accordance with mass balance calculations (see Table 1). These chemical changes are consistent with significant crystallization of pyrrhotite ± clinopyroxene in the reduced/moderately oxidized charges, whereas they are related to the crystallization of anhydrite + magnetite in the most oxidized charges (run 4).

Tiny spherical gold-rich blebs (generally about 1 μm in size, hereafter designated as Au-nuggets) were systematically found spatially associated with magnetite in all charges of the most oxidizing experiment (run 4). Several Au-nuggets slightly larger in size were also found in close textural association with pyrrhotite, anhydrite and fluid bubbles (Table 2 and Fig. 3c and d). According to their common spherical shape, these gold-rich particles are thought to have passed through a liquid state during the experiment. They indeed contain variable (though low) amounts of additional metals (mainly Pt, Pd, Cr, Ni). Simon et al. (2007) also reported the presence of Au nuggets in their experimental charges from the analysis of their LA-ICP-MS ablation signals. However, the authors did not observe such gold particles in their run products, probably due to their sub-micron size, and Simon et al. (2007) considered these Au nuggets to be quench phases. In contrast, our SEM observations (Fig. 3c and d) suggest that the Au nuggets in this study are phases stable under our experimental P and T. In fact, the Au nuggets are systematically associated with magnetite and pyrrhotite crystals and fluid bubbles, suggesting that their appearance is related to the oxide/sulfide crystallization mechanism on the one hand and to the precipitation of Au from the fluid phase during fluid dissolution in the melting rock powder, as proposed by Botcharnikov et al. (2010), on the other hand. Heterogeneous nucleation at experimental conditions might also be at the origin of Au nuggets since the presence of gold particles in contact with other solid phases proves that there is substantial transport of gold through melt; but even in this case, the nucleation process requires gold saturation of the silicate melt. Therefore the gold melt concentrations truly represent the solubility of gold at run conditions. As illustrated by Fig. 3, Au-nuggets in our experimental products can be as large as ~10 μm in diameter when in spatial association with sulfide crystals. Such grain sizes are unlikely for quench mineral phases, especially considering the characteristics of the quench in this study (isobaric and very fast, lasting <5 s). Therefore, we interpret the nuggets as having precipitated at experimental P and T, either from the fluid phase in the case of association with bubbles (Botcharnikov et al., 2010), or from a locally S–Fe–O-depleted, Au-saturated, 1–10 μm wide melt boundary layer generated during growth of sulfides and oxides. This interpretation provides the justification for not considering the Au spikes in the ICP-MS ablation signals for the calculation of the gold melt concentrations since the nuggets were probably not formed during quench (cf. [Botcharnikov et al., 2010] and [Jégo et al., 2010]). Attempts have been made to calculate the gold melt contents with considering the Au spikes related to the Au nuggets, but the results were inconsistent with each others and aberrant (in some charges, at least three orders of magnitude higher than the contents reported here), whereas gold contents calculated by filtering the Au spikes out are very consistent with those calculated from Au spike-free ablation signals of a given experimental glass. In addition, our gold concentrations are in the

same order of magnitude than those of Botcharnikov et al. (2010) who also filtered the Au spikes out of the ablation signals of their experimental glasses.

4.3. Sulfur concentrations in glasses

Sulfur concentrations in experimental glasses are detailed in Table 2. The distribution of sulfur contents as a function of fO_2, fS_2 and X_{Fe} for the three compositions is presented in Fig. 4.

In Fig. 4a, glass sulfur contents globally reproduce the classical inverted bell-shaped pattern of S solubility with varying fO_2 (e.g., Clemente et al., 2004). Under oxidizing conditions (above ~NNO+1), the S concentrations increase dramatically with increasing fO_2, from ~300 up to almost 2500 ppm, i.e., an increase of about one order of magnitude between ~NNO+1.25 and ~NNO+3.5. The high melt S solubility values under very oxidizing conditions strongly suggest dissolution of sulfur in the form of sulfate species (i.e., SO_4^{2-}). In contrast, the strong increase of melt S contents between NNO+1.25 and NNO+1.75 is likely due to the fact that, under oxidizing conditions, the highest S^{2-} concentrations in melt are reached in the narrow range of fO_2 at the sulfide–sulfate transition as a result of the progressive destabilization of sulfides, as shown by Botcharnikov et al. (2011). Indeed, the two charges from run 1 (Pin Dac composition) do not plot along this trend and show very low S contents at NNO+1.75–2.0; as discussed below (*cf*. Section 5.3.2), these significantly lower sulfur solubility values are interpreted to be the result of the rapid decrease of the melt S^{2-}/S^{6+} ratio from ~NNO+1.7. Under reducing conditions, glass S contents range from ~600 to 1200 ppm (or ~550 to 1750 ppm including data from run 5) at a nearly constant fO_2 around NNO−1. This wide range of S concentrations for a nearly constant fO_2 suggests that other parameters – such as fS_2, fH_2S, or the mole fraction of Fe^{2+} in melt – control S solubility. For instance, Clemente et al. (2004) report that the dependence of S solubility on fO_2 changes markedly with fS_2, which also may be the case in the present study. Also, the large variation of S concentrations in our reduced charges (run 6) may be related to the combined effects of decreasing melt FeO contents (Table 6) and increasing fH_2S (Table 2), as reported by Clemente et al. (2004) for sulfide-bearing charges.

In Fig. 4b, highly oxidized charges show very low fS_2 values and their melt S contents decrease with increasing fS_2, which confirms that in these glasses the main sulfur species is SO_4^{2-} and S dissolution is mostly controlled by fO_2. Both reduced and moderately oxidized charges show much higher fS_2 values (by more than four orders of magnitude). Moreover, the sulfur concentrations in the reduced ones seem to be positively correlated to fS_2, which is consistent with the hypothesis that S is principally dissolved as sulfide in these melts. Also, the observations made about the moderately oxidized glasses (i.e., S contents positively correlated with fO_2, but very high fS_2) confirm that sulfur in these charges is close to the transition sulfide/sulfate. Fig 4c shows that iron is only slightly fractionated from the melt in experiments performed above NNO+1 (the initial $\log(X_{Fe})$ of the starting compositions range between −1.57 and −1.44), to form either minor magnetite or sulfide mineral phases. In contrast, the reduced charges show significantly lower X_{Fe} values indicating a strong fractionation of iron to form pyrrhotite crystals, as confirmed by mass balance calculations (Table 2). The fact that melt S contents tend to increase with decreasing X_{Fe} in reducing conditions suggest that iron becomes too depleted in the silicate melt to crystallise additional sulfides, which facilitates the incorporation of sulfur into the melt. This observation has also been made by Clemente et al. (2004) in reduced rhyolitic experimental glasses.

No major difference in sulfur solubility was noted between the three compositions under reducing and moderately oxidizing conditions. As discussed above, only the non-adakitic charges (i.e., PhM5) are significantly S-enriched compared to the adakitic charges at ~NNO−1, most likely due to their higher fH$_2$S and very low FeO contents. Above ~NNO+3, S concentrations seem to correlate with the degree of adakitic imprint (i.e., value of bulk rock Sr/Y ratio; Table 1; *cf.* [Jégo et al., 2005] and [Jégo et al., 2010]) of the starting materials for a given fO$_2$ (i.e., [S]$_{Bal2}$ > [S]$_{Pin Dac}$ > [S]$_{PhM5}$). However, in these anhydrite-bearing charges, the NK/A ratio (i.e., molar (Na + K)/Al) of Bal2 melts is the highest (~0.70), followed by Pin Dac melts (~0.60) and then PhM5 melts (~0.50). Thus it appears that the degree of alkalinity of these melts is correlated to their degree of adakitic imprint. According to the experimental results of Scaillet and MacDonald (2006), melt sulfur contents are strongly dependent on the alkalinity of silicate melts; they report that peralkaline melts can, at all fO$_2$, dissolve 5–20 times more sulfur than their metaluminous equivalents. These observations therefore suggest that the differences in S solubility in our highly oxidized charges are related to their respective degree of alkalinity, rather than their adakitic imprint.

4.4. Gold concentrations in glasses

Gold contents in experimental glasses are presented in Table 2. Concentrations have been recalculated as mole fractions of Au dissolved in melt (X_{Au}) by using glass major element concentrations together with water and sulfur contents from Table 2 and Table 6 (mole fractions were calculated considering ten oxides – SiO$_2$, Al$_2$O$_3$, K$_2$O, Na$_2$O, CaO, FeO, MnO, MgO, TiO$_2$, Cr$_2$O$_3$ – plus elemental monoatomic sulfur, S, and Au, excluding H$_2$O).

The distribution of gold contents as a function of fO$_2$ for the three compositions is shown in Fig. 5. The first intuitive but important observation is that, in sulfur-bearing systems, gold behaves differently according to the redox state considered. Under reducing conditions (~NNO−1), gold contents vary greatly at sub-equal fO$_2$, ranging from ~1700 to ~5200 ppb (or from ~1000 ppb considering 'run 5' charges), i.e., by more than a factor of 3. Under moderately oxidizing conditions (~NNO+1.5), a very strong positive correlation is observed between melt Au contents and fO$_2$, with concentrations ranging from 865 to ~2500 ppb Au (i.e., by almost a factor of 3 too) over 0.35 log fO$_2$ unit only. Such a trend may suggest a mechanism of gold dissolution based on oxidized species (e.g., Au^{3+} or Au^{1+}) along this fO$_2$ range. As for sulfur (Fig. 4a), the two charges from run 1 show much lower gold contents, comparable to those observed under very oxidizing conditions (ΔNNO > 3) where gold concentrations (460–720 ppb) are the lowest of the experimental set and do not display any significant variation with increasing fO$_2$. Comparing the three starting compositions, no major difference in Au solubility is observed at given fO$_2$ under oxidizing conditions (ΔNNO > +1); only the PhM5 reduced charges (~4000–5200 ppb Au) are significantly more gold-enriched than the two other compositions (1700–3400 ppb Au), as also noted above for sulfur (Fig. 4).

Thus, from the preceding observations, it is worth stressing that (1) gold solubility in sulfur-bearing melts shows a larger scatter and reaches much higher values in reducing conditions than at fO$_2$ > ~NNO+1.75 and, (2) gold and sulfur behave similarly with varying fO$_2$ in reducing/moderately oxidizing conditions (i.e., ΔNNO < 2), but seem independent from each other under very high fO$_2$.

These important results are confirmed by the distribution of gold contents as a function of melt sulfur contents (Fig. 6a). A very well defined positive correlation is indeed observed between Au and S both in the reduced and moderately oxidized charges, with contents

ranging from ~250 to 5200 ppb and ~250 to 1200 ppm respectively. Such a trend strongly suggests an effective complexation between both elements in the melt over a wide range of fO_2 (at least $-1.5 < \Delta NNO < +2$). In contrast, melt gold concentrations display no variations with increasing sulfur content in highly oxidizing conditions. Fig. 6b shows a clear dependency of melt Au contents on fS_2 under reducing conditions, suggesting that gold dissolution is mainly controlled by fS_2, but no particular trend is observed in moderately and highly oxidizing conditions. Intermediate-fO_2 charges show fS_2 as high as the reduced ones, though, despite significantly lower melt Au contents; this likely confirms the presence of both oxidized gold species and Au–S complexes in this fO_2 range. The very low fS_2 values of the highly oxidized charges imply that at $\Delta NNO > 3$ Au dissolves either as oxidized gold species or/and as gold–sulfate complexes, but their low melt Au contents suggest that the mechanism of dissolution is much less efficient than in more reducing conditions. In Fig. 6c, the absence of correlation between X_{Fe} and melt Au contents in moderately and highly oxidized charges suggest that gold dissolution is not significantly influenced by the concentration of total iron. In contrast, the strong increase of gold solubility associated with decreasing X_{Fe} – and increasing melt S contents – in the reduced charges is consistent with complexation of gold with melt sulfide species while iron is sequestered into pyrrhotite crystals (*cf*. Section 4.3). Furthermore, this trend is inconsistent with a strong alloying of Fe with the Au capsule, which would lead to a decrease of the activity of metallic gold and would negatively affect its solubility in melt.

5. Discussion

5.1. Attainment of equilibrium

Electron microprobe analyses of experimental glasses and clinopyroxenes have standard deviations in most cases lower than analytical uncertainties (Table 3 and Table 6), indicating that these phases are homogeneous in terms of their major elements. All glasses, except some from 'run 5', also show homogeneous sulphur concentrations. For gold, the statistics of the Au analyses, detailed above, imply that gold is homogeneously distributed in our experimental glasses. Time-series runs performed by Bezmen et al. (1994) showed that gold equilibrates between sulfide and mafic/intermediate silicate melts after 30 h at 1250 °C and 4 kbar, for a silicate charge weighing 300–350 mg; even if our experimental temperature is significantly lower, the attainment of equilibrium in our charges is strongly supported by these results considering a run duration of 100 h and a silicate mass more than 10 times less. For H_2O in glasses, only bulk analytical data are available. However, multiple Karl–Fischer measurements were performed on each glass sample; absolute standard deviations ($\pm 2\sigma$) are generally <1 wt.%, indicating homogeneity. Considering that glass powders were used as starting materials, the experimental durations in this study (>100 h) and the diffusivity data for of H_2O in silicate melts of intermediate composition (Liu et al., 2004), water is expected to be homogeneously distributed in the experimental charges.

Nevertheless, it should be emphasized that all experimental glasses in this study attained their final gold concentrations from the low concentration side and that gold solubility was in no case approached from the high concentration side, since our Au concentration data have not been reversed. However, various lines of evidence, detailed below, suggest that the Au concentrations measured in the glasses can be considered as equilibrium solubilities at high P and T:

(1)   Gold concentrations in experimental glasses from this study vary by more than a factor of 20, ranging from 253 to 5159 ppb (Table 2). Gold concentrations in glasses correlate with the experimental parameters (Fig. 4), so that the variations in gold concentrations between samples can be ascribed to differences either in fO_2, fS_2, or S and FeO contents in the melt. This would be unexpected if Au concentrations in glasses were significantly influenced by kinetic factors. The ability of the melt to homogenize with respect to Au can be tested by considering the amount of time required for Au to diffuse through the melt at run conditions. To our knowledge, there are no experimental data for Au diffusivity in silicate liquids, but Mungall (2002b) report modeled Au diffusivities estimated in several magmatic systems, with values going from 2.7×10^{-7} to 1.5×10^{-5} cm^2 s^{-1} over a wide range of temperature (i.e., 1100–1600 °C). In our case, the section surface of our experimental charges is about 4.9 mm^2 (Au capsule inner diameter = 2.5 mm) and the run duration is on average of 3.6×10^5 s, which leads to a minimum Au diffusivity value of $\sim 1.36 \times 10^{-7}$ cm^2 s^{-1} for gold to diffuse throughout the whole silicate charge, i.e., twice lesser than the lowest Au diffusivity estimated by Mungall (2002b). These calculations strongly suggest that gold reached equilibrium in our experiments.

(2)   'Run 5' underwent an unusually slow quench, with a quench rate of the order of 50–100 °C s^{-1}. So, a "duplicate" experiment of same duration (run 6) was performed to check for reproducibility. Au contents in 'run 5' charges are on average slightly lower than in 'run 6' charges, but gold solubilities in these two experiments are mutually consistent and the results stress the direct dependence of gold solubilities either on glass S concentrations or fO_2. We interpret these statistically lower Au contents and the significant heterogeneity of S contents in some glasses of 'run 5' (Table 2) as a result of the slow quench, isobaric fluid exsolution leading to the formation of micro-bubbles (observable in SEM pictures) and to a partitioning of gold and sulfur from the melt to the fluid phase. Thus, gold analyses gave lower results because the Au spikes corresponding to the Au-enriched micro-bubbles were filtered out of the ablation signals (the calculated Au concentrations corresponding therefore to the locally Au-depleted residual melt), and sulfur analyses show some heterogeneity because the amount of S-enriched micro-bubbles hit by the electron beam was different for each analysis.

(3)   A fast quench device was used systematically. The Au nuggets present in some charges are interpreted to be stable phases present under our experimental P–T conditions and not precipitated during quench (the previous paragraph (2) shows that a slower quench rate does not lead to the formation of Au nuggets, but rather to fluid exsolution). Therefore, the gold concentration of the melt has not been modified during quench (except for 'run 5'), and we consider the Au concentration data to represent gold concentrations in the melts at high P and T.

5.2. Influence of sulfur on the solubility of gold: comparison with S-free data

Most previous S-free studies focused on the determination of the partitioning of gold between H_2O-saturated rhyolitic silicate melt, sulfide, oxide, and magmatic aqueous phases ([Frank et al., 2002], [Simon et al., 2003], [Simon et al., 2005] and [Simon et al., 2007]) rather than investigating its solubility in the melt. Besides, the experimental conditions or melt compositions of the few studies reporting gold solubility data always differ significantly from ours, making any comparison difficult (see Jégo et al., 2010). For example, the solubility of gold in S-free, Cl-bearing, H_2O-saturated haplogranitic melt at 800 °C, 1–1.5 kbar and fO_2 around NNO is estimated at $\sim$500 ppb ([Simon et al., 2003] and [Simon et al., 2005]), $\sim$1 ppm (Frank et al., 2002) and $\sim$2.5 ppm (Simon et al., 2007). Despite a significant heterogeneity, also noted by Botcharnikov et al. (2010), all these values do fit quite well with our Au concentration range in the presence of sulfur.
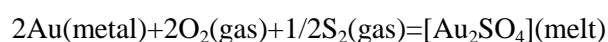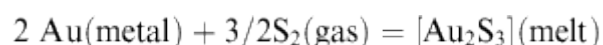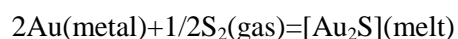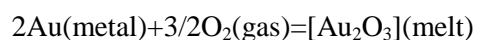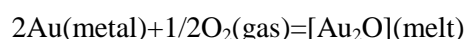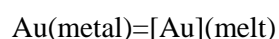
However, the S-bearing dataset of the present study is directly comparable to our recently published S-free data (Jégo et al., 2010), since the starting material compositions and the experimental conditions were the same. Melt gold contents are significantly enhanced by the presence of sulfur along the whole fO_2 range investigated in the two studies. However, it is worth stressing that the difference of gold contents between S-free and S-bearing glasses decreases with increasing fO_2. Under reducing conditions (~NNO−1 to 1.5), Au contents are substantially increased in S-bearing melts, by 1.5 up to 2 orders of magnitude compared to S-free melts. For more oxidizing conditions (~NNO+1.5 to 2.5), this difference becomes smaller, about 1.5 to 0.5 orders of magnitude. At ΔNNO > 3, gold contents in S-bearing melts are not distinguishable from the extrapolated gold contents in S-free charges (*cf.* Jégo et al., 2010), suggesting that the presence of sulfur dissolved mainly as sulfate species SO_4^{2-} does not influence significantly the solubility of gold in melt. Botcharnikov et al. (2011) also proposed that there is little difference in Au speciation between S-bearing and S-free systems under strongly oxidizing conditions.

Previous results of sulfur-bearing experiments in the literature are discussed below (Section 5.4).

5.3. Gold solubility and speciation in S-bearing silicate melts

5.3.1. Thermodynamic analysis of the solubility of Au in S-bearing silicate melts

Our gold solubility results were obtained at three discrete oxygen fugacities (Fig. 5), quite apart from each other (at least two log fO_2 units). Each set of data exhibits different absolute concentrations, scatter and dependence on fO_2, fS_2 and X_{Fe}. Since natural magmas may lie anywhere between, we aim to propose one unifying model for gold dissolution in intermediate magmatic melts in presence of S. Regarding the speciation of gold in silicate melt, little work has been done to date. Only Borisov and Palme (1996) suggest Au^{1+} as the stable species in their very oxidized ($10^{-7} < \log fO_2 < 10^{-3}$) S-free experimental silicate melts. They specify, though, that Au_2O_3 is known to be much more stable and is a common gold oxide. So, given the three valence states of gold observed in nature (i.e., Au^0, Au^{1+}, Au^{3+}) and the preceding observations on the behaviour of gold and sulfur with $fO_2/fS_2/X_{Fe}$ (*cf.* Sections 4.3 and 4.4), an appropriate set of dissolved species may include Au^0 (metal), Au_2^IO, $Au_2^{III}O_3$, Au_2^IS and $Au_2^{III}S_3$, all together with sulfate complexes $Au_2^ISO_4$ and $Au_2^{III}(SO_4)_3$, and iron sulfide complexes $Au_2^IFeS_2$ and $Au^{III}FeS_{2.5}$. Each species concentration is then related to the gold activity (saturating metal), system fugacities and FeS mole fraction in melt (X_{FeS}) as follows:

Au(metal)=[Au](melt)

2Au(metal)+1/2O₂(gas)=[Au₂O](melt)

2Au(metal)+3/2O₂(gas)=[Au₂O₃](melt)

2Au(metal)+1/2S₂(gas)=[Au₂S](melt)

$$2\ Au(metal) + 3/2S_2(gas) = [Au_2S_3](melt)$$

2Au(metal)+2O₂(gas)+1/2S₂(gas)=[Au₂SO₄](melt)

2Au(metal)+6O₂(gas)+3/2S₂(gas)=[Au₂(SO₄)₃](melt)

$$2Au(metal)+FeS(melt)+1/2S_2(gas)=[Au_2FeS_2](melt)$$

$$Au(metal)+FeS(melt)+3/4S_2(gas)=[AuFeS_{2.5}](melt)$$
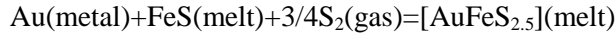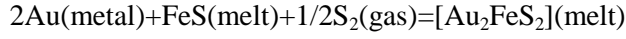
The measured gold solubilities in all experiments are a sum of abundances of all species present (on the right hand side), which are products of respective equilibrium constants and system variables $- fS_2$, fO_2 and X_{FeS}. In our experiments, melts were equilibrated with pure gold metal (since no alloying of Fe with Au from the capsule was observed). Therefore, the activity and the mole fraction of gold in the metal can be taken equal to unity, and the equilibrium constants K's corresponding to each equation at constant temperature and pressure can be written as follows:

$$\log K_9 = \log(X_{Au0}^{melt} \cdot \gamma_{Au0}^{\infty,melt})$$

$$\log K_{10} = \log(X_{Au_2O}^{melt} \cdot \gamma_{Au_2O}^{\infty,melt}) - 1/2 \log fO_2$$

$$\log K_{11} = \log(X_{Au_2O_3}^{melt} \cdot \gamma_{Au_2O_3}^{\infty,melt}) - 3/2 \log fO_2$$

$$\log K_{12} = \log(X_{Au_2S}^{melt} \cdot \gamma_{Au_2S}^{\infty,melt}) - 1/2 \log fS_2$$

$$\log K_{13} = \log(X_{Au_2S_3}^{melt} \cdot \gamma_{Au_2S_3}^{\infty,melt}) - 3/2 \log fS_2$$

$$\log K_{14} = \log(X_{Au_2SO_4}^{melt} \cdot \gamma_{Au_2SO_4}^{\infty,melt}) - 2\log fO_2 - 1/2\log fS_2$$

$$\log K_{15} = \log(X_{Au_2(SO_4)_3}^{melt} \cdot \gamma_{Au_2(SO_4)_3}^{\infty,melt}) - 6\log fO_2 - 3/2 \log fS_2$$

$$\log K_{16} = \log(X_{Au_2FeS_2}^{melt} \cdot \gamma_{Au_2FeS_2}^{\infty,melt}) - \log(X_{FeS}^{melt} \cdot \gamma_{FeS}^{\infty,melt}) - 1/2 \log fS_2$$

$$\log K_{17} = \log(X_{AuFeS_{2.5}}^{melt} \cdot \gamma_{AuFeS_{2.5}}^{\infty,melt}) - \log(X_{FeS}^{melt} \cdot \gamma_{FeS}^{\infty,melt}) - 3/4 \log fS_2$$

where $X_j$melt and $\gamma_j^{\infty,melt}$ are the mole fraction and the activity coefficient of gold species j dissolved in the silicate melt, and X_{FeS}^{melt} and $\gamma_{FeS}^{\infty,melt}$ are the mole fraction and the activity coefficient of FeS in silicate melt. At given temperature T and pressure P, log K is constant. If we assume that log $\gamma_j^{\infty,melt}$ is independent of the concentration of species j dissolved in the melt, and of fS_2, fO_2 and T (but not necessarily of the melt composition), it follows that:

$$\log X_{Au0}^{melt} = C_9$$

$$\log X_{Au_2O}^{melt} = 1/2 \log fO_2 + C_{10}$$

$$\log X_{Au_2O_3}^{melt} = 3/2 \log fO_2 + C_{11}$$

$$\log X_{Au_2S}^{melt} = 1/2\log fS_2 + C_{12}$$

$$\log X_{Au_2S_3}^{melt} = 3/2\log fS_2 + C_{13}$$

$$\log X_{Au_2SO4}^{melt} = 2 \log fO_2 + 1/2 \log fS_2 + C_{14}$$

$$\log X^{\text{melt}}_{\text{Au}_2(\text{SO}_4)3} = 6 \log f\text{O}_2 + 3/2 \log f\text{S}_2 + C_{15}$$

$$\log X^{\text{melt}}_{\text{Au}_2\text{FeS}_2} = \log X_{\text{FeS}} + 1/2 \log f\text{S}_2 + C_{16}$$

$$\log X^{\text{melt}}_{\text{Au}_2\text{FeS}_{2.5}} = \log X_{\text{FeS}} + 3/4 \log f\text{S}_2 + C_{17}$$

where $C_j = \log K_j - \log \gamma_j^{\infty,\text{melt}}$ (thus C_j is constant for a given melt composition), $C_{16} = \log K_{16} - \log \gamma_{\text{Au}_2\text{FeS}_2}^{\infty,\text{melt}} - \log \gamma_{\text{FeS}}^{\infty,\text{melt}}$, and $C_{17} = \log K_{17} - \log \gamma_{\text{AuFeS}_{2.5}}^{\infty,\text{melt}} - \log \gamma_{\text{FeS}}^{\infty,\text{melt}}$.

Note that the hypothesis of $\log \gamma_j^{\infty,\text{melt}}$ being independent of the species j concentration in the melt is equivalent to assume that gold dissolution follows Henry's law for our investigated ranges of gold concentration, T, $f\text{O}_2$ and $f\text{S}_2$.

Eqs. (27), (28), (29), (30), (31), (32), (33), (34) and (35) have been fitted simultaneously to all our experimental gold solubility data (except run 5). We assumed that $X_{\text{FeS}} \approx X_{\text{S}}$ (Table 2), i.e., the reduced sulfur is linked exclusively to iron (and to negligible amounts of gold) in the silicate melt, which is a reasonable hypothesis for our melt compositions. The constants C_j (Appendix A.3, Table S1 and S2) were determined by linear regression from our solubility data at different $f\text{O}_2$, $f\text{S}_2$ and X_{FeS} i.e., their respective values were estimated by least-square minimization of the difference between measured and calculated X_j^{melt} (e.g., Albarède, 1995). Then, the bulk gold solubility ($X_{\text{Au}}^{\text{melt}}$) is the sum of abundances of all dissolved gold species j present in the silicate melt i:

(36)

$$X^{\text{melt}}_{\text{Au}} = \sum X^{\text{melt}}_{ij}$$

5.3.2. Results of the thermodynamic model

Results of the model are illustrated in Fig. 7, Fig. 8 and Fig. 9. Fig. 7 shows that calculated gold contents are in excellent agreement ($R^2 = 0.97$) with the measured concentrations. All experimental data are satisfactorily reproduced by the model within less than a 0.14 log X_{Au} unit difference, with 80% of the charges showing a difference $\leqslant 0.06$ log X_{Au} unit. This almost perfect agreement data-model is also illustrated in Fig. 8 as a function of the three key parameters log $f\text{O}_2$ (a), log $f\text{S}_2$ (b) and log X_{Fe} (c). It appears that all different trends described by the data and discussed above are very well reproduced by the model. The largest differences are observed for very oxidizing conditions, eventually suggesting that some oxidized gold species were omitted from our thermodynamic analysis.

Table S2 (matrix of solutions C; Appendix A.3) shows that the calculated $10^{\wedge}C_{12}$, $10^{\wedge}C_{14}$ and $10^{\wedge}C_{17}$ have negative values, implying that the constants C can not be determined. The geochemical interpretation of these results is that the corresponding gold species (Au_2S, Au_2SO_4 and $\text{AuFeS}_{2.5}$, respectively) are not present in the experimental silicate melts. All other species considered in the thermodynamic analysis (i.e., Au (metal), Au_2O, Au_2O_3, Au_2S_3, $\text{Au}_2(\text{SO}_4)_3$ and Au_2FeS_2) have positive $10^{\wedge}C_j$, therefore they are supposedly present in our experimental glasses in variable proportions. The quality of the agreement suggests that the three parameters considered in the model – log $f\text{O}_2$, log $f\text{S}_2$ and log X_{FeS} – are the main variables controlling the dissolution of gold in melt under our experimental PTX conditions.

Several other modelling attempts have been made with more basic sets of gold species, notably by avoiding the sulfide and sulfate gold complexes (from Eqs. (14), (15), (16) and (17)), but this led to much less efficient agreements between measured and calculated Au concentrations. This stresses the importance of such complexes in the mechanism of gold dissolution, as discussed below.

The absence of Au_2SO_4 and $AuFeS_{2.5}$ species in the experimental silicate melts, as mentioned above, seems quite intuitive since it is likely due to the relative poor thermodynamic stability of ambivalent Au–S–(Fe) complexes involving reduced gold Au^{1+} and sulfate species on the one hand, and oxidized gold Au^{3+} and sulfide species on the other hand. In contrast, the absence of Au_2S may appear more surprising since this species is intuitively expected to account for a major part of gold dissolution in reduced S-bearing silicate melts. However in Fig. 9, which shows the relative proportion of the different gold species dissolved in the melt as a function of $\log fO_2$ (calculated from Eq. (36); see Appendix A.3), a very large part (~76–92%) of gold is dissolved as Au_2FeS_2 under reducing to moderately oxidizing conditions (~$\log fO_2 < -8.6$). The absence of Au_2S associated to this predominance of Au_2FeS_2 strongly suggests that in sulfide-saturated, Fe-bearing silicate melts gold is principally attached to Fe–S complexes rather than to S alone. In other words, sulfur S^{2-} complexes firstly with Fe^{2+} then accepts Au^{1+}, but does not complex with gold alone to form Au_2S if Fe^{2+} is present and available in the melt. Besides, the strong increase of Au_2FeS_2 from $\log fO_2 \sim -9.1$ to -8.6 (Fig. 9) is consistent with the increase of S^{2-} solubility in melt at the sulfide–sulfate transition (resulting from the progressive destabilization of sulfides) as shown by Botcharnikov et al. (2011) and suggested above to account for the increase of our melt S solubility data under moderately oxidizing conditions (*cf*. Section 4.3).

In addition to the dominant Au_2FeS_2 species, gold dissolution under reducing to moderately oxidizing conditions is accounted for by relatively small percentages of Au metal (<22% of total Au) and Au_2S_3 species (<16% of total Au) (Fig. 9). Importantly, however, the proportion of Au_2S_3 at ~NNO−1 ($\log fO_2 \sim -11.3$) is much lower (<6%), i.e., the proportion of Au_2S_3 species increases with fO_2, implying a decrease of Au^{1+}/Au^{3+} ratio with increasing fO_2. Also, the strong increase of S^{2-} concentrations in melt at intermediate fO_2 likely favours the formation of Au_2S_3, and explains why a fraction of S^{2-} complexes with gold alone while the proportion of Au_2FeS_2 rapidly increases.

At $\log fO_2 > -8.6$, the melt S^{2-}/S^{6+} ratio rapidly decreases at the expense of Au_2FeS_2 species whose proportion drops to ~52% at $\log fO_2 \sim -8.25$ (Fig. 9). This leads to a very significant decrease of the melt Au solubility over a narrow fO_2 range (see run 1 in Fig. 5). Fig. 9 shows however that this Au solubility drop is partly compensated by the formation of $Au_2(SO_4)_3$ species up to ~30% of total Au, and by minor amounts of Au metal, Au_2S_3 and Au_2O. This corresponds to a decrease of Au^{1+}/Au^{3+} ratio in melt from >22 to 1.5 between $\log fO_2 \sim -8.6$ and -8.25.

Under very oxidizing conditions ($\log fO_2 > -7.4$), the main part of gold is dissolved as Au metal in silicate melt (Fig. 9), stressing the inefficiency of the mechanism of gold dissolution in sulfate-saturated silicate melts. However the proportion of Au^0 decreases rapidly from ~70% to 42% with increasing fO_2 to the benefit of Au^{3+} species, i.e., $Au_2(SO_4)_3$ and Au_2O_3 (up to ~17% and 13%, respectively, at $\log fO_2 \sim -6.75$). Under such oxidizing conditions, Au^{1+} species are almost totally represented by Au_2O which accounts for ~22–28% of total Au (Fig. 9). A small proportion (<5%) of Au_2FeS_2 still remains at $\log fO_2 \sim -7.4$ but no longer exists at $\log fO_2 \sim -6.75$. The evolution of the relative proportions of Au^{1+} species (i.e.,

$Au_2O + Au_2FeS_2$) and Au^{3+} species (i.e., $Au_2(SO_4)_3 + Au_2O_3$) between $\log fO_2 \sim -7.4$ and -6.75 leads to a decreasing melt Au^{1+}/Au^{3+} ratio from ~ 0.9 to 0.45. At the same time, the ratio ($Au^{1+} + Au^{3+}$)/Au metal of total gold dissolved in melt evolves from 0.3 to almost 0.6, while the melt Au solubility remains quasi-constant.

Interestingly, the consideration of AuO_xS_y species (i.e., gold thiosulfates) in the thermodynamic analysis does not improve or significantly alter the quality of the data-model agreement; models involving thiosulfate species lead to very similar results than those described above, both quantitatively and qualitatively, with determination coefficients $R^2 = 0.92$–0.97 depending on the species considered ($Au_4^{I}OS_3$, $Au_2^{III}O_3S$ and $Au_2^{III}OS_2$). For instance, the Au_4OS species may be considered in the model according to the equation:

$$4Au(metal) + 1/2 O_2(gas) + \frac{1}{2} S_2(gas) = [Au_4OS](melt)$$
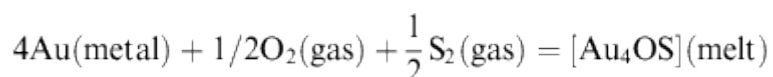
the thiosulfate species is only present in moderately oxidizing conditions, between 5 and 10 wt.% (not shown), which notably induces a light decrease of the proportion of Au_2FeS_2. Also, the consideration of Au_4OS modifies to some extent the relative proportions of the gold species present in very oxidizing conditions, in particular Au_2O proportion goes down to 14–17% while Au_2O_3 and $Au_2(SO_4)_3$ proportions significantly increase up to 30% and 19%, respectively, at $\log fO_2 \sim -6.75$.

Results with thiosulfate clearly stress the need for spectroscopic data on the speciation of Au in silicate melts.

5.4. Comparison with previous S-bearing solubility data

As already mentioned, most previous studies focused on the determination of the partitioning of gold between Au metal, rhyolitic or basaltic melts, coexisting magmatic aqueous phases and sulfides (either crystalline or molten) in S-bearing magmatic assemblages ([Bezmen et al., 1994], [Fleet et al., 1996], [Fleet et al., 1999], [Crocket et al., 1997], [Jana and Walker, 1997], [Jugo et al., 1999], [Simon et al., 2007], [Simon et al., 2008] and [Bell et al., 2009]) rather than providing Au solubility data. Though, Simon et al. (2007) reported Au solubility of about 600 ppb in H_2O-saturated rhyolitic melt at $\sim$NNO, and Jugo et al. (2005a) measured a solubility on the order of $\sim$500 ppb Au in anhydrous basaltic melt (1300 °C, 10 kbar) under reducing conditions. Bezmen et al. (1994) reported a gold concentration of $\sim$800 ppb in a Bushweld Complex melt ($\sim$56 wt.% SiO_2) saturated with H–C–O–S fluids (1300 °C, 4 kbar, $\sim$NNO), but Au activity was not equal to unity in their experiments. Those three values are noticeably lower than our own results at NNO-1 ($\sim$FMQ-0.4), but the two first ones are similar to our most oxidized data and the third one is comparable to the lowest value of our moderately oxidized dataset (865 ppb Au). On the other hand, Jugo et al. (1999) reported a gold solubility of about 4 ± 2 ppm in hydrous haplogranitic melt (850 °C, 1 kbar) under reducing conditions that fits very well with our highest solubility values ($\sim$4–5 ppm). Recently, Botcharnikov et al. (2010) presented the first experimental Au solubility data in S-bearing hydrous intermediate (i.e., andesitic) silicate melts near NNO. Similarly to our study, their data suggest a positive correlation between the concentrations of Au and S dissolved in the melt under reducing/moderately oxidizing conditions. They reported lower Au and S solubilities in the melt, from 300 to 2500 ppb Au and 0–400 ppm S, but such values are consistent with the lower end of the trend described by our reduced/moderately oxidized data in Fig. 6a and suggest fS_2 values lower in Botcharnikov et al. (2010) than in the present experiments.

As pointed out in the previous section, our gold solubility results are also in good agreement with those of Botcharnikov et al. (2011). Fig. 10a shows the gold solubility curve vs. fO_2 in our dacitic melts corresponding to the interpretation of our experimental results and thermodynamic model (data of Botcharnikov et al. (2011) in basaltic and andesitic melts are shown for comparison). We report a maximum Au solubility under moderately oxidizing conditions corresponding to the sulfide/sulfate transition (at log (fO_2) ~ −8.65 or ~NNO+1.5). As indicated by Figs. 4a, 6a and 9, this increase of gold solubility is the consequence of an increase of the concentration of S^{2-} species in the melt that results from the destabilization of sulfides. The low Au solubilities in run 1 charges at log (fO_2) ~ −8.4 result from the rapid decrease of S^{2-}/S^{6+} ratio in melt at the end of the transition sulfide–sulfate which induces a drop of sulfur (and so gold) solubility in melt. With further increasing fO_2 the solubility of sulfur in melt is strongly enhanced whereas the solubility of gold remains low (<0.7 ppm Au). Botcharnikov et al. (2011) also show a maximum Au solubility at the transition sulfide–sulfate (Fig. 10a); however, they report it at ~FMQ+1 in basaltic melts and at ~FMQ+1.25 in andesitic melts (i.e., ~NNO+0.3 and ~NNO+0.5, respectively, under the PT conditions of their study, 0.2 GPa and 1050 °C), well below the maximum observed in the present study (~NNO+1.5 at 0.4 GPa and 1000 °C). Many attempts have been made in the literature to determine S speciation in natural magmas/glasses and locate precisely the position of the sulfide–sulfate transition in various silicate melt compositions as a function of fO_2 (e.g., Métrich et al., 2009 and references therein). Recent work by Jugo (2009) and [Jugo et al., 2005b] and [Jugo et al., 2010] show that the sulfide–sulfate transition occurs around FMQ+1 in basaltic compositions, which corresponds to the observations of Botcharnikov et al. (2011). However, Moretti and Baker (2008) report the sulfide–sulfate transition at fO_2 as high as NNO+2 in H_2O-saturated rhyolitic melts at 800 °C and 0.5 GPa, and show that the fO_2 at which the calculated sulfate species becomes the dominant species in the melt changes by two orders of magnitude as composition, pressure, temperature, and water concentration change. The difference of fO_2 at which the transition occurs in basaltic and rhyolitic melts is due to compositional effects on the activities of the sulfide and sulfate species dissolved in the melt ([Moretti and Baker, 2008] and [Baker and Moretti, 2011]). Our moderately oxidized charges, anyway, are sulfide-saturated (*cf.* Table 2) and fall in the pyrrhotite field of the fO_2 vs. fS_2 diagram calculated at the experimental PTX conditions (Fig. 1), attesting that the corresponding silicate melts are still on the sulfide side of the S^{2-}/S^{6+} transition. Moreover, the fact that the charge C4A plots just on the right of the pyrrhotite/anhydrite boundary in Fig. 1 (or just on the boundary, considering the error in fO_2) confirms that the run 1 charges recorded exactly the sulfide–sulfate transition, which theoretically occurs at $\log fO_2$ ~ −8.35 (~NNO+1.9) at $\log fS_2$ ~ + 2.5, T = 1000 °C and P = 0.4 GPa, in Pinatubo-like dacitic compositions.

The theoretical gold solubility at constant fS_2 and X_{FeS} calculated from our model as a function of fO_2 is shown in Fig. 10b. It appears that Au solubility is absolutely constant for given values of fS_2 and X_{FeS} along the fO_2 range corresponding to sulfide saturation. Our calculations also show that an increase of fS_2 and/or X_{FeS} leads to a significant increase of Au solubility consistent with our observations and interpretations relative to the sulfide destabilization at the sulfide–sulfate transition and the associated increase of S^{2-} species in the melt. Under oxidizing conditions (i.e., at sulfate saturation), such high values for $\log fS_2$ (0 or 1) are not realistic; as a consequence, the model artifactually predicts a hollow of Au solubility due to a virtual increase of Au_2SO_4 species, followed by a dramatic increase of Au solubility due to the enhanced formation of $Au_2(SO_4)_3$ species. Obviously such artefacts do not correspond to the reality and, therefore, they are not reproduced by our data whose $\log fS_2$ are much lower (−2.50 to −3.80; Table 2 and Fig. 6b).

Under reducing conditions (log fO_2 < NNO+1), pyrrhotite mineral phases are very stable and buffer the sulfur concentration in silicate melt at a low level (few hundreds ppm), leading to a low solubility of gold in melt, typically <1 ppm under low fS_2 and X_{FeS} (*cf.* grey and pink dotted lines in Fig. 10b). With decreasing fO_2, the stability and the proportion of sulfide minerals increase and the activity of Fe in melt decreases significantly. Our experimental charges from run 6 at log (fO_2) < −11 confirm this trend, showing up to 5 wt.% pyrrhotite crystals (Table 2) and melt FeO concentrations going from 0.82 down to 0.25 wt.% (Table 6). At such low melt FeO contents and under reducing conditions (log fO_2 < NNO+1), a strong increase of melt S contents is commonly observed, that is principally controlled by the increase of fH_2S (e.g., [O'Neill and Mavrogenes, 2002] and [Clemente et al., 2004]). This is consistent with what is observed in run 6 charges which show a dramatic increase of both melt S and Au concentrations with increasing fH_2S (Table 2 and Fig. 10a).

Thus, our results as well as those of Botcharnikov et al. (2011) show that sulfide undersaturation of the primary magmas or/and highly oxidizing conditions, which are widely assumed to be prerequisite factors for metal mobilization from the source, are actually not required. It appears that the most favourable conditions for the generation of Au-enriched magmas are expected either at the sulfide/sulfate transition through destabilization of sulfides or under reducing conditions in Fe-poor, S-rich melts at equilibrium with iron sulfides.

6. Implications for the gold budget of arc magmas

The key role of sulfur in the formation of major subduction-related epithermal and porphyry-type Au–Cu–Mo deposits has been suggested in many studies (e.g., [Sillitoe, 1997], [Hattori and Keith, 2001], [Kesler et al., 2002], [Imai, 2002], [Imai, 2004], [Mungall, 2002a] and [Mungall, 2002b]). The present experimental study confirms, together with the recent results of [Botcharnikov et al., 2010] and [Botcharnikov et al., 2011], the significant effect of the presence of sulfur on the solubility of gold in silicate melts, and provides important results for understanding the genesis of Au deposits.

Our data show (1) very high gold solubilities under reducing conditions (<NNO−1) in Fe-poor, S-rich, sulfide-saturated melts due to the increase of fH_2S, and (2) a strong increase of gold solubility at the sulfide/sulfate transition (from ~NNO+1.2 to NNO+1.5) due to the destabilization of sulfides and the increase of melt S^{2-} concentration, in agreement with the calculations of Moretti and Baker (2008) and the experimental results of Botcharnikov et al. (2011). Many hydrous calc-alkaline arc magmas are highly oxidized, with fO_2 between FMQ+1 (~NNO+0.3) and FMQ+3 (~NNO+2.3) (e.g., [Behrens and Gaillard, 2006] and [Jugo et al., 2010]), and it is commonly suggested that rocks from the mantle wedge are slightly more reduced than the produced arc magmas (e.g., Parkinson and Arculus, 1999) with typical fO_2 from FMQ+0.4 (~NNO−0.3) to FMQ+1.7 (~NNO+1). Thus, the fO_2 range representative of most of primary arc magmas overlaps the fO_2 range at which the sulfide/sulfate transition and the associated maximum Au solubility occur. Therefore, during the genesis and the early evolution of primary arc melts rising through the mantle wedge, the Au concentration in silicate melt is critically constrained by the variation of fO_2 and related melt S^{2-} concentration.

Along with magma fractionation and decompression, the exsolution of aqueous fluids generally causes the fO_2 of the melt to increase owing to the mass transfer of hydrogen from the melt to the volatile phase (e.g., Candela, 1986). This process has been termed "self-oxidation" or "auto-oxidation". In addition, a decrease in pressure will tend to increase the

bulk Fe^{3+}/Fe^{2+} ratio of the magma and then promote relative oxidation (e.g., Ballhaus, 1993). The magnitude of fO_2 increase will drop with increasing oxidation, but fO_2 will never decrease unless some exotic process occurs such as assimilation of reduced material. The self-oxidation process relates to the stability of sulfide minerals (and ferromagnesian phases) which may be resorbed upon oxidation, hence destabilization of sulfides (e.g., Nadeau et al., 2010). Halter et al. (2002) (and subsequent Halter papers) discussed this process with respect to the evolving metal budget of ore-generative arc magmas. The self-oxidation process will lead to the destabilization of pyrrhotite if fO_2 increases beyond the sulfide–sulfate transition, i.e., above NNO in mafic and NNO+2 in felsic melts ([Mungall, 2002a], [Mungall, 2002b], [Moretti and Baker, 2008] and [Jugo, 2009]). Therefore, a primitive basaltic melt formed around NNO−NNO+1 and rising up through the mantle wedge is very likely to cross the sulfide–sulfate transition during the early stages of its degassing and fractionation. In contrast, a more silicic primary melt (typically dacitic or rhyolitic, e.g., from low-degree slab partial melting) formed in the same redox conditions will have to undergo a greater increase in fO_2 – i.e., more degassing and more decompression – to reach the sulfide–sulfate transition (Fig. 10a). According to our data and those of Botcharnikov et al. (2011), gold solubility in the melt reaches a maximum just before S^{6+} species become dominant, implying that – if enough gold is present in the system and available to the melt – the primary magma may become particularly Au-enriched with increasing melt S^{2-} content before complete destabilization of sulfides. Then, with increasing fO_2 during magma evolution and as soon as the S^{6+} species become dominant in the melt, both sulfur and gold solubilities drop rapidly, possibly leading to a S- and Au-oversaturated melt. At this point, excess gold might form immiscible Au-nuggets but most of it is likely to be transferred massively to the exsolving fluid phase, together with excess sulfur dissolved mainly as SO_2. Such early Au- and S-rich magmatic fluids may represent ideal vectors for the formation of major ore deposits. Nevertheless, it is interesting to note that an evolving melt may remain close to its maximum Au solubility if the increase in fO_2 occurs simultaneously with the evolution of the melt towards more felsic compositions. In this case, the distribution of gold is expected to be constrained by the partition coefficients of gold between fluid phase, sulfide phase and silicate melt in the P–T–fO_2–fS_2 conditions, until the sulfide–sulfate transition is eventually passed.

In the particular case of reduced magmas ($fO_2 <$ NNO−1) – which is not commonly observed in subduction zone settings, very high gold solubilities can be reached in Fe-poor, sulfide-saturated melts as shown in Fig. 10a. The wide range of high Au solubilities observed at constant fO_2 is associated to a wide range of high S solubilities related to a variable increase of fH_2S. If a primary melt forms under such reducing conditions at equilibrium with very stable sulfides, it may become Au-enriched during partial melting of the source depending on the fH_2S (and the availability of Au and S in the source). Then, as the magma evolves, the fO_2 increase is expected to induce a decrease of fH_2S and a drop of melt S (and so Au) solubility down to a level where the sulfur concentration in melt is controlled principally by the presence of sulfides (i.e., SCSS). Therefore the degassing melt becomes rapidly S- and Au-oversaturated, and the excess gold and sulfur massively transfer to the exsolving fluid phase, similarly to the sulfide–sulfate transition but in the stability field of sulfides.

In summary, this study shows that gold enrichment in evolving arc magmas and associated fluid phases is likely to occur over a wide range of fO_2 at sulfide saturation, from $\log(fO_2) <$ NNO−1 to the sulfide–sulfate transition, i.e., ~NNO+0.5–2.0. In contrast, sulfide–undersaturation and very oxidizing conditions (ΔNNO > +2) do not appear to be favourable to the formation of ore-bearing fluids, unless extremely high fO_2 (ΔNNO > +3.5) are reached (Fig. 10a) which is not commonly observed, even in subduction zone settings.

However, it is worth stressing that the lowest Au solubility contents of our dataset – measured in anhydrite-bearing charges and in sulfide-saturated charges from run 1 – are as high as 500–700 ppb. Such concentrations are 20–50 times higher than the Au contents of our natural starting materials, and up to two orders of magnitude higher than those measured in the most fresh arc rocks (e.g., [Connors et al., 1993] and [Polvé et al., 2004]). Moreover, those solubility values are measured in melts in equilibrium with Ti-poor magnetite, which is reported to moderately sequester Au from a crystallizing silicate melt with a partition coefficient, $D_{Au}^{mgt/melt} \approx 4$ (Simon et al., 2003; see also Jenner et al., 2010). Therefore, a calc-alkaline arc melt is unlikely to reach gold solubility and saturation during magma fractionation and degassing, unless the magma source is particularly Au- and S-enriched and the transfer of gold to the partial melt efficient enough.

In order to estimate the gold budget of calc-alkaline arc magmas, let us consider a typical mantle wedge partial melt. The global upper mantle contains 1.5 ppb Au (e.g., [Mitchell and Keays, 1981], [Lorand et al., 1999], [McInnes et al., 1999] and [Borisov and Palme, 2000]), but in Archean greenstones and modern oceanic basalts, typical background Au contents are 0.7–2 ppb ([Meyer and Saager, 1985], [Greenough and Fryer, 1990] and [Togashi and Terashima, 1997]). Loucks and Mavrogenes (1999) report solubility values of 29 and 167 ppm Au at 0.37 GPa and 625 °C in supercritical hydrothermal brines equilibrated with pyrrhotite + magnetite. Such solubility concentrations are extremely high, and the slab-derived fluids are not expected to be Au-saturated. Loucks and Mavrogenes (1999) consider that, with 100% extraction efficiency, fluids emitted from rocks such as Archean greenstones and modern oceanic basalts by amphibolite devolatilization reactions would contain ⩽0.2 ppm Au. To our knowledge, this value represents the only estimates in the literature for the gold concentration in potential analogues of the aqueous phases supposedly emanating from dehydration of the subducted slab. If we assume that a few wt.% of the mantle wedge are metasomatized by such dehydration fluids, then the bulk metasomatized sub-arc mantle may contain at the most around 5 ppb Au, mainly as (Cu)-Fe sulfide minerals and, in a lesser extent, as metal alloys and metal oxides. We assume complete precipitation of gold during metasomatism, since the metasomatizing fluids will end up in being totally consumed by reaction with the mantle rocks. Then we consider a fractional melting from 1% to 20% of the mantle wedge, and we assume that most of all Au will be consumed during partial melting because (1) Au-bearing phases are located in or in the vicinity of the metasomatic veins and are surrounded by hydrous minerals (amphiboles, serpentines) which will first be destabilized during partial melting, (2) the main Au-bearing mineral phases are sulfides (pyrrhotite, chalcopyrite, pyrite) which are likely to be totally destabilized during fractional melting under increasing fO$_2$ between ∼NNO−0.5 and NNO+2 depending on the melt composition, (3) a highly incompatible behaviour is assumed for gold (Borisova et al., 2006), and (4) extremely low gold concentrations are generally found in mantle rocks (∼1.5 ppb Au; e.g., Lorand et al., 1999) which indicates that gold is not efficiently preserved in the residue. Taking into account that the partitioning of gold is controlled exclusively by (Cu)–Fe-sulfides (negligibly small partition coefficients of Au are reported between other mineral phases of the mantle and silicate melts; Brenan et al., 2005), we consider an initial abundance of sulfides in the mantle to be about 690 ppm (that is, 250 ppm S; McDonough and Sun, 1995) and a sulfide/silicate melt partition coefficient for Au of 200 (estimated from the range of $D_{Au}^{sulfide/silicate}$ measured by Botcharnikov et al. (2011) at ΔFMQ ± 1 and 1050 °C). Thus, 1–20% fractional melting of a mantle with an initial Au concentration of 5 ppb would lead to a batch of primitive calc-alkaline basaltic melt containing a maximum range of 56–68 ppb Au after complete destabilization/melting of sulfides. Even if such melt gold concentrations seem high for

natural samples, they are three orders of magnitude lower than the maximum Au solubilities measured by Botcharnikov et al. (2011) and one order of magnitude lower than our gold solubility data at log (fO$_2$) $\geqslant$ NNO+2 (Fig. 5). During subsequent magma evolution and rise through the mantle wedge and the arc crust, that primitive mafic magma will likely undergo a fractionation of potential Au-sequestering phases, like magnetite (for which Simon et al. (2003) report a small gold partition coefficient from the melt, $D_{\mathrm{Au}}^{\mathrm{mgt/melt}} \approx 4$) and, above all, degassing of a Au-rich magmatic aqueous phase. The fluid/melt partition coefficients for Au will depend critically on the absolute chlorinity/salinity of the aqueous phase, the pressure, and the temperature. However, even with considering a quite low partition coefficient of ~12 for gold between low-salinity vapor and S-saturated rhyolitic melt (Simon et al., 2007; 800 °C/0.12 GPa), several wt.% of degassed magmatic fluids lead to lower the gold concentrations in melt by more than one order of magnitude. Such estimations are consistent with the literature data about natural gold contents in "regular" (i.e., not particularly Au-enriched) calc-alkaline magmas, typically around 2–3 ppb (e.g., [Connors et al., 1993] and [Polvé et al., 2004]), but still significantly lower than the bulk gold contents measured in our starting materials (12–38 ppb Au; Table 1).

In contrast, the partial melting (in similar conditions than described above) of a mantle containing only 1 ppb – as used by Botcharnikov et al. (2011) in their fractional melting model – leads to gold contents of only 11–14 ppb in the primitive melt. After potential crystallisation of Au-bearing oxides and continuous degassing of Au-rich aqueous phases, these initial melt gold concentrations seem too low to account for natural gold contents in most of "regular" evolved calc-alkaline arc magmas.

These estimations were made for a typical calc-alkaline sub-arc mantle melt and, therefore, represent the lower limit of gold contents in common arc magmas. It is worth to explore, though, the case of more particular arc magmas which are believed to involve the products of slab partial melting in their petrogenesis, a hypothesis still being debated concerning the origin of the 1991 Pinatubo dacite. Jégo et al. (2010) proposed that the petrogenetic models involving slab partial melting may potentially lead to an enrichment of Au and S in melt compared to typical calc-alkaline magmas. They calculated that 5–20% partial melting of the bulk massive (Cu)–Fe-sulfide–bearing slab may result in a sulfur-rich slab melt with Au content ranging between 300 and 1200 ppb. These very high concentrations are about one order of magnitude lower than the maximum Au solubility measured by Botcharnikov et al. (2011) at ~FMQ+1 (~NNO+0.3), but are comparable to the lowest values of our solubility data at NNO+1.2–1.5 (Fig. 5). This implies that gold concentrations as high as ~1 ppm may be reached in slab partial melts under fO$_2$ conditions characteristic of the mantle wedge. If magma evolution leads to increase fO$_2$ beyond NNO+2, the melt gold concentration may be limited to ~500–700 ppb though. Such high solubility limits allow particular arc magmas – notably those whose petrogenesis involves slab partial melting – to be significantly Au-enriched (even after intensive degassing and fractionation of Au-bearing oxide phases) and to exsolve ore-forming Au–S-rich fluid phases. The gold contents measured in the bulk anhydrous Pinatubo dacite (12 ppb Au; this study) and in its hydrous rhyolitic groundmass (22 ppb Au; Borisova et al., 2006), as well as those of our two other starting materials Bal2 (38 ppb Au) and PhM5 (29 ppb Au) can easily be explained by these estimations.

Despite the lack of data in the literature on the partitioning of Au and S between the slab and slab-derived supercritical aqueous fluids and partial melts, our calculations point out the importance to consider a magma source particularly enriched in gold (and sulfur), i.e., either the mantle wedge metasomatized by slab-derived fluids/melts, or the slab itself, to account for

the natural gold contents of most of typical calc-alkaline arc magmas. In addition, our experimental data show that Au-enrichment may occur over a wide range of fO$_2$ at sulfide–saturation but is critically controlled by variations of fS$_2$ and fH$_2$S; this may be used to constrain models of ore-forming processes from evolved calc-alkaline arc magmas associated with major Au–Cu–Mo deposits.

7. Conclusions

The new data presented here show that, in a sulfur-bearing dacitic system, (1) the solubility of gold in silicate melt is drastically enhanced compared to S-free systems (by up to two orders of magnitude), (2) very high gold solubilities are reached under reducing conditions (<NNO−1) in Fe-poor, S-rich, sulfide-saturated melts due to the increase of fH$_2$S, and (3) a strong increase of gold solubility occurs at the sulfide/sulfate transition (from ∼NNO+1.2 to NNO+1.5) due to the destabilization of sulfides and the increase of melt S^{2-} concentration, in agreement with the calculations of Moretti and Baker (2008) and the experimental results of Botcharnikov et al. (2011). Thermodynamic modeling of our data suggests that the dissolution of gold in silicate melt is the result of a combination of several gold species (Au metal, Au$_2$O, Au$_2$O$_3$, Au$_2$S$_3$, Au$_2$(SO$_4$)$_3$ and Au$_2$FeS$_2$) dissolved in the melt in variable proportions, depending on the three parameters considered in the model – log fO$_2$, log fS$_2$ and log X_{FeS} – which are the main variables controlling the dissolution of gold in melt under the experimental PTX conditions. According to our modeling results, Au$_2$FeS$_2$ is the main gold species dissolved in reducing conditions (i.e., S^{6+}/S$_{total}$ ∼ 0), whereas at sulfate saturation gold is mainly dissolved as Au metal and Au$_2$O. The present study shows that sulfide undersaturation of the primary magmas or/and highly oxidizing conditions, which are widely assumed to be prerequisite factors for metal mobilization from the source, are actually not required. Instead, gold enrichment in evolving arc magmas and exsolving fluid phases is likely to occur over a wide range of fO$_2$ at sulfide saturation, from log(fO$_2$) < NNO−1 to the sulfide–sulfate transition (i.e., NNO+0.5–2.0), but is critically controlled by variations of fS$_2$ and fH$_2$S. Fractional melting calculations show that metasomatism of the mantle wedge by Au-enriched, slab-derived aqueous fluids may be a possible scenario to account for the gold contents of typical calc-alkaline arc magmas, but suggest that slab partial melting is required for the generation of Au-enriched magmas. Indeed, the abundance of sulfur in the magma source (and therefore the nature/composition of the source) is proposed to be a main factor controlling the enrichment of gold in arc magmas associated to major Au–Cu–Mo deposits.

Appendix A

A.1. Determination of fS_2 in highly oxidized charges. Calculation of the field boundaries between anhydrite and magnetite in fO_2–fS_2 space

The fS_2 in highly oxidized charges was determined from mineral–melt equilibria involving the anhydrite ($CaSO_4$) + magnetite (Fe_3O_4) assemblage. The calculation is conceptually identical to that performed by Luhr (1990). However, in our experiments, cpx never crystallizes together with anhydrite + magnetite. Therefore, the equilibrium reaction of Luhr (1990) must be rewritten in terms of the silicate components of the melt instead of the cpx:

(A1)

$$CaSiO_{3(melt)} + 2/3\,Fe_3O_{4(magnetite)} + 1/2\,S_{2(gas)} + 7/6\,O_{2(gas)}$$
$$= CaSO_4(anhydrite) + Fe_2SiO_{4(melt)}$$
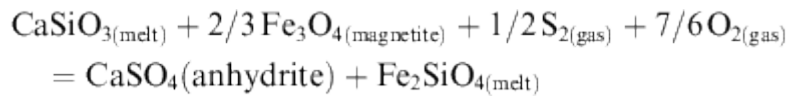
The equilibrium constant for reaction (A1) is:

(A2)

$$K = (a_{Fe_2SiO_4}/a_{CaSiO_3}) \cdot (1/(fS_2^{1/2} \cdot fO_2^{7/6} \cdot a_{Fe_3O_4}^{2/3}))$$

where $a_{Fe2SiO4}$ and a_{CaSiO3} are the activities of the components Fe_2SiO_4 and $CaSiO_3$ in the silicate melt, respectively, and a_{Fe3O4} is the activity of the component Fe_3O_4 in magnetite. Anhydrite is considered as a pure phase. Then the fS_2 can be expressed as:

(A3)

$$\log fS_2 = 2(-\log K + \log(a_{Fe_2SiO_4}/a_{CaSiO_3}) - 7/6 \log fO_2$$
$$- \log(a_{Fe_3O_4}^{2/3}))$$

The activities of the melt components and of Fe_3O_4 in magnetite under our experimental conditions can be estimated by using the MELTS software ([Ghiorso and Sack, 1995] and [Asimow and Ghiorso, 1998]), using compositional data for coexisting magnetite and melts from Table 4 and Table 6. The equilibrium constant for reaction (A1) can also be written as:

(A4)

$$Ln K = -\Delta G_{P,T}^{\circ}/\,RT$$

where the G terms for the melt components and Fe_3O_4 in magnetite are calculated with MELTS. For anhydrite, S_2 and O_2, the G terms are calculated from Majzlan et al. (2002) and Robie and Hemingway (1995), respectively.

Once the $\log K$ value is known, $\log fS_2$ can be determined as a function of fO_2 using compositional data (Table 4 and Table 6) and fO_2 specific to each charge. Results are shown on Fig. 1.

A.2. Calculation of the field boundaries between pyrrhotite and anhydrite and pyrrhotite and magnetite in fO_2–fS_2 space

The boundary between pyrrhotite (FeS) and anhydrite in a log (fO_2) vs. log (fS_2) diagram (Fig. 1) was calculated with the same method outlined above using the relation:

(A5)

$$2CaSiO_{3(melt)}+2FeS_{(pyrrhotite)}+4O_{2(gas)}=2CaSO_{4(anhydrite)}+Fe_2SiO_4(melt)+SiO_{2(melt)}$$
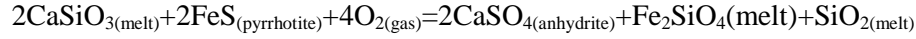
The equilibrium constant for reaction (A5) is:

(A6)

$$K = (a_{Fe_2SiO_4} \cdot a_{SiO_2}/a^2_{CaSiO_3}) \cdot (1/(fO_2^4 \cdot a^2_{FeS}))$$

where $a_{Fe2SiO4}$, a_{SiO2} and a_{CaSiO3} are the activities of the melt components Fe_2SiO_4, SiO_2 and $CaSiO_3$, respectively (estimated by using MELTS and compositional data from Table 6), and a_{FeS} is the activity of the FeS component in pyrrhotite.

The equilibrium constant for reaction (A5) can also be written as:

(A7)

$$\mathrm{Ln}K = -\Delta G^{\circ}_{P,T}/RT$$

where the G terms are calculated as above for the melt components and anhydrite and from Robie and Hemingway (1995) for pyrrhotite. Once the constant K has been determined, a_{FeS} is calculated from Eq. (A6) by specifying fO_2. Then fS_2 is obtained from a_{FeS} (Froese and Gunter, 1976) and the fO_2–fS_2 pairs along the pyrrhotite–anhydrite field boundary determined.

The boundary between pyrrhotite and magnetite in a log (fO_2) vs. log (fS_2) diagram (Fig. 1) was calculated from the equilibrium reaction between these two mineral phases, according to the relation:

(A8)

$$3FeS_{(pyrrhotite)}+2O_{2(gas)}=Fe_3O_{4(magnetite)}+3/2S_{2(gas)}$$
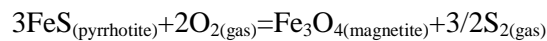
The equilibrium constant for reaction (A8) is:

(A9)

$$K = (a_{Fe_3O_4} \cdot fS_2^{3/2}) \cdot (1/(a^3_{FeS} \cdot fO_2^2))$$

where a_{FeS} and a_{Fe3O4} are the activities of the component FeS in pyrrhotite and the component Fe_3O_4 in magnetite, respectively. They are both estimated with MELTS. Compositional data are taken from Table 4 and Table 5. The equilibrium constant for reaction (A8) can also be written as:

(A10)

$$\text{Ln} K = -\Delta G^{\circ}_{P,T}/RT$$

Again, the G's are calculated as outlined above and the value of the constant K can be determined. Then, fO_2–fS_2 pairs corresponding to the boundary between the stability fields of pyrrhotite and magnetite can be calculated from Eq. (A9).

A.3. Determination of the constants C_j

In Table S1, the equations for the calculation of the constants C_j are given for each gold species j. A_{ij} is the matrix of the abundances of all gold species j expressed in terms of fO_2, fS_2 and X_{FeS} (according to Eqs. (27), (28), (29), (30), (31), (32), (33), (34) and (35)) dissolved in every experimental glass i. Let A_t be the transposed matrix of A_{ij}, and B the matrix of the measured gold mole fractions, then the matrix of solutions C is expressed as $C = [((At·A)−1)·At]·B$. The resulting values of the C_j (i.e., expressed as $10^{\wedge}C_j$) obtained from our dataset are reported in Table S2; these values are then used to calculate the total gold mole fraction in every charge i (log X_i Au; bottom row of Table S1) according to Eq. (36). It is worth noting that these constants C are only valid for our P, T conditions and the compositional range covered by our starting materials.

References

Albarède, 1995 F. Albarède Introduction to Geochemical Modelling Cambridge University Press (1995)

Ancey et al., 1978 M. Ancey, F. Bastenaire, R. Tixier Applications des méthodes statistiques en microanalyse Microanalyse, microscope électronique à balayage, Edition de physique, Orsay, France (1978), pp. 323–347

Aries et al., 2000 S. Aries, M. Valladon, M. Polve, B. Dupre A routine method for oxide and hydroxide interference corrections in ICPMS chemical analysis of environmental and geological samples Geostand. Newslett., 24 (2000), pp. 19–31

Asimow and Ghiorso, 1998 P.D. Asimow, M.S. Ghiorso Algorithmic modifications extending MELTS to calculate subsolidus phase relations Am. Mineral., 83 (1998), pp. 1127–1131

Baker and Moretti, 2011 D.R. Baker, R. Moretti Modeling the solubility of sulfur in magmas: a 50-year old geochemical challenge Rev. Mineral. Geochem., 73 (2011), pp. 167–213

Ballhaus, 1993 C. Ballhaus Redox states of lithospheric and asthenospheric mantle Contrib. Mineral. Petrol., 114 (1993), pp. 331–348

Behrens, 1995 H. Behrens Determination of water solubilities in high viscosity melts: an experimental study on $NaAlSi_3O_8$ and $KAlSi_3O_8$ melts Eur. J. Mineral., 7 (1995), pp. 905–920

Behrens and Gaillard, 2006 H. Behrens, F. Gaillard Geochemical aspects of melts: volatiles and redox behavior Elements, 2 (2006), pp. 275–280

Behrens et al., 1996 H. Behrens, C. Romano, M. Nowak, F. Holtz, D.B. Dingwell Near-infrared spectroscopic determination of water species in glasses of the system $MAlSi_3O_8$ (M = Li, Na, K): an inter-laboratory study Chem. Geol., 128 (1996), pp. 41–63

Bell et al., 2009 A. Bell, A. Simon, M. Guillong Experimental constraints on Pt, Pd and Au partitioning and fractionation in silicate melt-sulfide–oxide-aqueous fluid systems at 800 °C, 150 MPa and variable sulfur fugacity Geochim. Cosmochim. Acta, 73 (2009), pp. 5778–5792

Bellon and Yumul, 2000 H. Bellon, G.P. Yumul Jr. Mio-Pliocene magmatism in the Baguio Mining District (Luzon, Philippines): age clues to its geodynamic setting C.R. Acad. Sci. Paris, 331 (2000), pp. 295–302

Bellon and Yumul, 2001 H. Bellon, G.P. Yumul Jr. Miocene to quaternary adakites and related rocks in Western Philippine arc sequences C.R. Acad. Sci. Paris, 333 (2001), pp. 343–350

Bezmen et al., 1994 N.I. Bezmen, M. Asif, G.E. Brügmann, I.M. Romanenko, A.J. Naldrett Distribution of Pd, Rh, Ru, Ir, Os, and Au between sulfide and silicate melts Geochim. Cosmochim. Acta, 58 (1994), pp. 1251–1260

Borisov and Palme, 1996 A. Borisov, H. Palme Experimental determination of the solubility of Au in silicate melts Mineral. Petrol., 56 (1996), pp. 297–312

Borisov and Palme, 2000 A. Borisov, H. Palme Solubilities of noble metals in Fe-containing silicate melts as derived from experiments in Fe-free systems Am. Mineral., 85 (2000), pp. 1665–1673

Borisova et al., 2006 A.Y. Borisova, M. Pichavant, M. Polvé, M. Wiedenbeck, R. Freydier, F. Candaudap Trace element geochemistry of the 1991 Mt. Pinatubo silicic melts, Philippines: implications for ore-forming potential of adakitic magmatism Geochim. Cosmochim. Acta, 70 (2006), pp. 3702–3716

Botcharnikov et al., 2010 R.E. Botcharnikov, R.L. Linnen, F. Holtz Solubility of Au in Cl- and S-bearing hydrous silicate melts Geochim. Cosmochim. Acta, 74 (2010), pp. 2396–2411

Botcharnikov et al., 2011 R.E. Botcharnikov, R.L. Linnen, M. Wilke, F. Holtz, P.J. Jugo, J. Berndt High gold concentrations in sulphide-bearing magma under oxidizing conditions Nat. Geosci., 4 (2011), pp. 112–115

Brenan et al., 2005 J.M. Brenan, W.F. McDonough, R. Ash An experimental study of the solubility and partitioning of iridium, osmium and gold between olivine and silicate melt Earth Planet. Sci. Lett., 237 (2005), pp. 855–872

Burnham, 1979 C.W. Burnham The importance of volatile constituents H.S. Yoder Jr. (Ed.), The Evolution of the Igneous Rocks: Fiftieth Anniversary Perspectives, Princeton University Press, Princeton (1979), p. 439 (Chapter 16)

Candela, 1986 P.A. Candela The evolution of vapor from silicate melts: effect on oxygen fugacity Geochim. Cosmochim. Acta, 50 (1986), pp. 1205–1211

Chou, 1986 I.-M. Chou Permeability of precious metals to hydrogen at 2 kb total pressure and elevated temperatures Am. J. Sci., 286 (1986), pp. 638–658

Clemente et al., 2004 B. Clemente, B. Scaillet, M. Pichavant The solubility of sulphur in hydrous rhyolitic melts J. Petrol., 45 (2004), pp. 2171–2196

Connors et al., 1993 K.A. Connors, D.C. Noble, S.D. Bussey, S.I. Weiss Initial gold contents of silicic volcanic rocks: bearing on the behaviour of gold in magmatic systems Geology, 21 (1993), pp. 937–940

Crocket et al., 1997 J.H. Crocket, M.E. Fleet, W.E. Stone Implications of composition for experimental partitioning of platinum-group elements and gold between sulfide liquid and basalt melt: the significance of nickel content Geochim. Cosmochim. Acta, 61 (1997), pp. 4139–4149

Di Carlo et al., 2006 I. Di Carlo, M. Pichavant, S.G. Rotolo, B. Scaillet Experimental crystallization of a high-K arc basalt: the golden pumice, stromboli volcano (Italy) J. Petrol., 47 (2006), pp. 1317–1343

Fleet et al., 1996 M.E. Fleet, J.H. Crocket, W.E. Stone Partitioning of platinum-group elements (Os, Ir, Ru, Pt, Pd) and gold between sulfide liquid and basalt melt Geochim. Cosmochim. Acta, 60 (1996), pp. 2397–2412

Fleet et al., 1999 M.E. Fleet, J.H. Crocket, M. Liu, W.E. Stone Laboratory partitioning of platinum-group elements (PGE) and gold with application to magmatic sulfide–PGE deposits Lithos, 47 (1999), pp. 127–142

Frank et al., 2002 M.R. Frank, P.A. Candela, P.M. Piccoli, M.D. Galscock Gold solubility, speciation and partitioning as a function of HCl in the brine-silicate melt-metallic gold system at 800 °C and 100 MPa Geochim. Cosmochim. Acta, 66 (2002), pp. 3719–3732

Froese and Gunter, 1976 E. Froese, A.E. Gunter A note on the pyrrhotite–sulfur vapour equilibrium Econ. Geol., 71 (1976), pp. 1589–1594

Ghiorso and Sack, 1995 M.S. Ghiorso, R.O. Sack Chemical mass transfer in magmatic processes. IV. A revised and internally consistent thermodynamic model for the interpolation and extrapolation of liquid–solid equilibria in magmatic systems at elevated temperatures and pressures Contrib. Mineral. Petrol., 119 (1995), pp. 197–212

Greenough and Fryer, 1990 Greenough J. D. and Fryer B. J. (1990) Distribution of gold, palladium, platinum, rhodium, ruthenium, and iridium in leg 115 hotspot basalts: implications for magmatic processes. In *Proceedings of the Ocean Drilling Program, Scientific Results, College Station, TX (Ocean Drilling Program)*, (eds. R. A Duncan, J Backmann and L. C Peterson), vol. 115, pp. 71–84.

Gunter et al., 1987 M.D. Gunter, J. Myers, S. Girsperberg Hydrogen: metal membranes H.L. Barnes, G.C. Ulmer (Eds.), Hydrothermal Experimental Techniques, Wiley, New York (1987), pp. 100–120

Halter et al., 2002 W.E. Halter, T. Pettke, C.A. Heinrich The origin of Cu/Au ratios in porphyry-type ore deposits Science, 296 (2002), pp. 1844–1846

Harris et al., 2003 A.C. Harris, V.S. Kamenetsky, N.C. White, E. van Achterbergh, C.G. Ryan Melt inclusions in veins: linking magmas and porphyry Cu deposits Science, 302 (2003), pp. 2109–2111

Hattori and Keith, 2001 K.H. Hattori, J.D. Keith Contribution of mafic melt to porphyry copper mineralization: evidence from Mount Pinatubo, Philippines, and Bingham Canyon, Utah, USA Mineral. Deposita, 36 (2001), pp. 799–806

Hedenquist and Lowenstern, 1994 J.W. Hedenquist, J.B. Lowenstern The role of magmas in the formation of hydrothermal ore deposits Nature, 370 (1994), pp. 519–527

Holtz et al., 1992 F. Holtz, H. Behrens, D.B. Dingwell, R.P. Taylor Water solubility in alumino-silicate melts of haplogranite composition at 2 Kbar Chem. Geol., 96 (1992), pp. 289–302

Holtz et al., 1995 F. Holtz, H. Behrens, D.B. Dingwell, W. Johannes H_2O solubility in haplogranitic melts: compositional, pressure, and temperature dependence Am. Mineral., 80 (1995), pp. 94–108

Imai, 2001 A. Imai Generation and evolution of ore fluids for porphyry Cu–Au mineralization of the Santo Tomas II (Philex) deposit, Philippines Res. Geol., 51 (2001), pp. 71–96

Imai, 2002 A. Imai Metallogenesis of porphyry Cu deposits of the western Luzon arc, Philippines: K–Ar ages, SO_3 contents of microphenocrystic apatite and significance of intrusive rocks Res. Geol., 52 (2002), pp. 147–161

Imai, 2004 A. Imai Variation of Cl and SO_3 contents of microphenocrystic apatite in intermediate to silicic igneous rocks of Cenozoic Japanese island arcs: implications for porphyry Cu metallogenesis in the Western Pacific island arcs Res. Geol., 54 (2004), pp. 357–372

Jana and Walker, 1997 D. Jana, D. Walker The influence of sulfur on partitioning of siderophile elements Geochim. Cosmochim. Acta, 61 (1997), pp. 5255–5277

Jégo et al., 2005 S. Jégo, R.C. Maury, M. Polvé, G.P. Yumul Jr., H. Bellon, R.A. Tamayo Jr., J. Cotton Geochemistry of adakites from the Philippines: constraints on their origins Res. Geol., 55 (2005), pp. 163–187

Jégo et al., 2010 S. Jégo, M. Pichavant, J.A. Mavrogenes Controls on gold solubility in arc magmas: an experimental study at 1000 °C and 4 kbar Geochim. Cosmochim. Acta, 74 (2010), pp. 2165–2189

Jenner et al., 2010 F.E. Jenner, H.St.C. O'Neill, R.J. Arculus, J.A. Mavrogenes The magnetite crisi in the evolution of arc-related magmas and the initial concentration of Au, Ag and Cu J. Petrol., 51 (2010), pp. 2445–2464

Jugo et al., 1999 P.J. Jugo, P.A. Candela, P.M. Piccoli Magmatic sulfides and Au:Cu ratios in porphyry deposits: an experimental study of copper and gold partitioning at 850 °C, 100 MPa in a haplogranitic melt-pyrrhotite-intermediate solid solution-gold metal assemblage, at gas saturation Lithos, 46 (1999), pp. 573–589

Jugo et al., 2005a P.J. Jugo, R.W. Luth, J.P. Richards, P.J. Sylvester, M.N. Tubrett Experimental determination of the solubilities of Ir, Pt, Pd and Au in sulfide- and sulfate-saturated basaltic melts at 1300 °C and 1 GPa: implications for HSE fractionation in subduction zones Geophys. Res. Abs., 7 (2005), p. 04879

Jugo et al., 2005b P.J. Jugo, R.W. Luth, J.P. Richards Experimental data on the speciation of sulfur as a function of oxygen fugacity in basaltic melts Geochim. Cosmochim. Acta, 69 (2005), pp. 497–503

Jugo, 2009 P.J. Jugo Sulfur content at sulfide saturation in oxidized magmas Geology, 37 (2009), pp. 415–418

Jugo et al., 2010 P. Jugo, M. Wilke, R.E. Botcharnikov Sulfur K-edge XANES analysis of natural and synthetic basaltic glasses: implications for S speciation and S content as function of oxygen fugacity Geochim. Cosmochim. Acta, 74 (2010), pp. 5926–5938

Keays and Skinner, 1989 R.R. Keays, B.J. Skinner Introduction to: the geology of gold deposits: the perspective in 1988 R.R. Keays, W.R.H. Ramsay, D.I. Groves (Eds.), Economic Geology Monograph 6, The Economic Geology Publishing Company (1989)

Kesler et al., 2002 S.E. Kesler, S.L. Chryssoulis, G. Simon Gold in porphyry copper deposits: its abundance and fate Ore Geol. Rev., 21 (2002), pp. 103–124

Linnen et al., 1995 R.L. Linnen, M. Pichavant, F. Holtz, S. Burgess The effect of fO$_2$ on the solubility, diffusion, and speciation of tin in haplogranitic melt at 850 °C and 2 kbar Geochim. Cosmochim. Acta, 59 (1995), pp. 1579–1588

Liu et al., 2004 Y. Liu, Y. Zhang, H. Behrens H$_2$O diffusion in dacitic melts Chem. Geol., 209 (2004), pp. 327–340

Lorand et al., 1999 J.-P. Lorand, L. Pattou, M. Gros Fractionation of platinum-group elements and gold in the upper mantle: a detailed study in Pyrenean orogenic lherzolites J. Petrol., 40 (1999), pp. 957–981

Loucks and Mavrogenes, 1999 R.R. Loucks, J.A. Mavrogenes Gold solubility in supercritical hydrothermal brines measured in synthetic fluid inclusions Science, 284 (1999), pp. 2159–2163

Luhr, 1990 J.F. Luhr Experimental phase relations of water- and sulphur-saturated arc magmas and the 1982 eruptions of El Chichon volcano J. Petrol., 31 (1990), pp. 1071–1114

Majzlan et al., 2002 J. Majzlan, A. Navrotsky, J.M. Neil Energetics of anhydrite, barite, celestine, and anglesite: a high-temperature and differential scanning calorimetry study Geochim. Cosmochim. Acta, 66 (2002), pp. 1839–1850

Martel et al., 1999 C. Martel, M. Pichavant, F. Holtz, B. Scaillet, J.-L. Bourdier, H. Traineau Effects of fO$_2$ and H$_2$O on andesite phase relations between 2 and 4 kbar J. Geophys. Res., 104 (1999), pp. 29453–29470

Mathur et al., 2000 R. Mathur, J. Ruiz, S. Titley, S. Gibbins, W. Margotomo Different crustal sources for Au-rich and Au-poor ores of the Grasberg Cu–Au porphyry deposit Earth Planet. Sci. Lett., 183 (2000), pp. 7–14

Matthews et al., 1999 S.J. Matthews, D.H.S. Moncrieff, M.R. Carroll Empirical calibration of the sulphur valence oxygen barometer from natural and experimental glasses: method and applications Mineral. Mag., 63 (1999), pp. 421–431

McDonough and Sun, 1995 W.F. McDonough, S.S. Sun The composition of the Earth Chem. Geol., 120 (1995), pp. 223–253

McInnes et al., 1999 B.I.A. McInnes, J.S. McBride, N.J. Evans, D.D. Lambert, A.S. Andrew Osmium isotope constraints on ore metal recycling in subduction zones Science, 286 (1999), pp. 512–516

Métrich et al., 2009 N. Métrich, A.J. Berry, H.St.C. O'Neill, J. Susini The oxidation state of sulfur in synthetic and natural glasses determined by X-ray absorption spectroscopy Geochim. Cosmochim. Acta, 73 (2009), pp. 2383–2399

Meyer and Saager, 1985 M. Meyer, R. Saager The gold content of some Archaean rocks and their possible relationship to epigenetic gold–quartz vein deposits Mineral. Deposita, 20 (1985), pp. 284–289

Mitchell and Keays, 1981 R.H. Mitchell, R.R. Keays Abundance and distribution of gold, palladium and iridium in some spinel and garnet lherzolites: implications for the nature and origin of precious metal-rich intergranular components in the upper mantle Geochim. Cosmochim. Acta, 45 (1981), pp. 2425–2433 2435–2442

Moretti and Baker, 2008 R. Moretti, D.R. Baker Modeling the interplay of fO_2 and fS_2 along the FeS–silicate melt equilibrium Chem. Geol., 256 (2008), pp. 286–298

Mungall, 2002a J.E. Mungall Roasting the mantle: slab melting and the genesis of major Au and Au-rich Cu deposits Geology, 30 (2002), pp. 915–918

Mungall, 2002b J.E. Mungall Kinetic controls on the partitioning of trace elements between silicate and sulfide liquids J. Petrol., 43 (2002), pp. 749–768

Nadeau et al., 2010 O. Nadeau, A.E. Williams-Jones, J. Stix Sulphide magma as a source of metals in arc-related magmatic hydrothermal ore fluids Nat. Geosci., 3 (2010), pp. 501–505

Ohmoto and Kerrick, 1977 H. Ohmoto, D.M. Kerrick Devolatilisation equilibria in graphitic systems Am. J. Sci., 277 (1977), pp. 1013–1044

O'Neill and Mavrogenes, 2002 H.St.C. O'Neill, J.A. Mavrogenes The sulfide capacity and the sulfur content at sulfide saturation of silicate melts at 1400 °C and 1 bar J. Petrol., 43 (2002), pp. 1049–1087

Parkinson and Arculus, 1999 I.J. Parkinson, R.J. Arculus The redox state of subduction zones: insights from arc-peridotites Chem. Geol., 160 (1999), pp. 409–423

Polvé et al., 2004 Polvé M., de Parseval P., Jégo S. and Maury R. C. (2004) Where is the gold in adakites: preliminary results from a EPMA-SIMS study. 57-OSE-A1547, *Joint AOGS 1st Annual Meeting and second APHW Conference*, vol. 1, pp. 166 (abstr).

Polvé et al., 2007 M. Polvé, R.C. Maury, S. Jégo, H. Bellon, A. Margoum, G.P. Yumul Jr., B. Payot, R.A. Tamayo Jr., J. Cotton Temporal geochemical evolution of Neogene

magmatism in the Baguio gold-copper mining district (Northern Luzon, Philippines) Resour. Geol., 57 (2007), pp. 197–218

Pownceby and O'Neill, 1994 M.I. Pownceby, H. O'Neill Thermodynamic data from redox reactions at high temperature. III. Activity–composition relations in Ni–Pd alloys from EMF measurements at 850–1250 K, and calibration of the NiO + Ni − Pd assemblage as a redox sensor Contrib. Mineral. Petrol., 116 (1994), pp. 327–339

Prouteau and Scaillet, 2003 G. Prouteau, B. Scaillet Experimental constraints on the origin of the 1991 Pinatubo dacite J. Petrol., 44 (2003), pp. 2203–2241

Prouteau et al., 2000 G. Prouteau, R.C. Maury, F.G. Sajona, J. Cotton, J.-L. Joron Behaviour of Niobium, Tantalum and other high field strength elements in adakites and related lavas from the Philippines Island Arc, 9 (2000), pp. 487–498

Robie et al., 1978 R.A. Robie, B.S. Hemingway, J.R. Fisher Thermodynamic properties of minerals and related substances at 198.15 K and 1 bar (10^5 Pascals) pressure and at higher temperature Geol. Surv. Bull., 1452 (1978), p. 456

Robie and Hemingway, 1995 R.A. Robie, B.S. Hemingway Thermodynamic properties of minerals and related substances at 298.15 K and 1 bar (10^5 Pascals) pressure and at higher temperatures US Geol. Survey Bull., 2131 (1995), p. 461

Roux and Lefèvre, 1992 J. Roux, A. Lefèvre A fast-quench device for internally heated pressure vessels Eur. J. Mineral., 4 (1992), pp. 279–281

Sajona and Maury, 1998 F.G. Sajona, R.C. Maury Association of adakites with gold and copper mineralization in the Philippines C.R. Acad. Sci. Paris Earth Planet. Sci., 326 (1998), pp. 27–34

Scaillet and MacDonald, 2006 B. Scaillet, R. MacDonald Experimental and thermodynamic constraints on the sulphur yield of peralkaline and metaluminous silicic flood eruptions J. Petrol., 47 (2006), pp. 1413–1437

Scaillet et al., 1992 B. Scaillet, M. Pichavant, J. Roux, G. Humbert, A. Lefevre Improvements of the Shaw membrane technique for measurement and control of fH_2 at high temperatures and pressures Am. Mineral., 77 (1992), pp. 647–655

Scaillet et al., 1995 B. Scaillet, M. Pichavant, J. Roux Experimental crystallisation of leucogranite magmas J. Petrol., 36 (1995), pp. 663–705

Schmidt et al., 1997 B.C. Schmidt, F. Holtz, B. Scaillet, M. Pichavant The influence of H_2O–H_2 fluids and redox conditions on melting temperatures in the haplogranite system Contrib. Mineral. Petrol., 126 (1997), pp. 386–400

Sillitoe, 1989 R.H. Sillitoe Gold deposits in western Pacific island arcs: the magmatic connection R.R. Keays, W.R.H. Ramsay, D.I. Groves (Eds.), The Geology of Gold Deposits: The Perspective in 1988. Economic Geology Monograph, 6Economic Geology Publishing Co (1989), pp. 274–291

Sillitoe, 1997 R.H. Sillitoe Characteristics and controls of the largest porphyry copper–gold and epithermal gold deposits in the circum-Pacific region Aust. J. Earth Sci., 44 (1997), pp. 373–388

Sillitoe and Bonham, 1990 R.H. Sillitoe, H.F. Bonham Jr. Sediment-hosted gold deposits: distal products of magmatic–hydrothermal systems Geology, 18 (1990), pp. 157–161

Simon et al., 2003 A.C. Simon, T. Pettke, P.A. Candela, P.M. Piccoli, C.A. Heinrich Experimental determination of Au solubility in rhyolite melt and magnetite: constraints on magmatic Au budgets Am. Miner., 88 (2003), pp. 1644–1651

Simon et al., 2005 A.C. Simon, M.R. Frank, T. Pettke, P.A. Candela, P.M. Piccoli, C.A. Heinrich Gold partitioning in melt–vapor–brine systems Geochim. Cosmochim. Acta, 69 (2005), pp. 3321–3335

Simon et al., 2007 A.C. Simon, T. Pettke, P.A. Candela, P.M. Piccoli, C.A. Heinrich The partitioning behaviour of As and Au in S-free and S-bearing magmatic assemblages Geochim. Cosmochim. Acta, 71 (2007), pp. 1764–1782

Simon et al., 2008 A.C. Simon, P.A. Candela, P.M. Piccoli, M. Mengason, L. Englander The effect of crystal-melt partitioning on the budgets of Cu, Au, and Ag Am. Mineral., 93 (2008), pp. 1437–1448

Sun et al., 2004 W. Sun, R.J. Arculus, V.S. Kamenetsky, R.A. Binns Release of gold-bearing fluids in convergent margin magmas prompted by magnetite crystallization Nature, 431 (2004), pp. 975–978

Taylor et al., 1992 J.R. Taylor, V.J. Wall, M.I. Pownceby The calibration and application of accurate redox sensors Am. Mineral., 77 (1992), pp. 284–295

Togashi and Terashima, 1997 S. Togashi, S. Terashima The behavior of gold in unaltered island arc tholeiitic rocks from Izu-Oshima, Fuji, and Osoreyama volcanic areas, Japan Geochim. Cosmochim. Acta, 61 (1997), pp. 543–554

Truckenbrodt and Johannes, 1999 J. Truckenbrodt, W. Johannes H_2O loss during piston–cylinder experiments Am. Mineral., 84 (1999), pp. 1333–1335

Ulrich et al., 1999 T. Ulrich, D. Günther, C.A. Heinrich Gold concentrations of magmatic brines and the metal budget of porphyry copper deposits Nature, 399 (1999), pp. 676–679

Westrich, 1987 H.R. Westrich Determination of water in volcanic glasses by Karl–Fischer titration Chem. Geol., 63 (1987), pp. 335–340

White and Hedenquist, 1990 N.C. White, J.W. Hedenquist Epithermal environments and styles of mineralization: variations and their causes, and guidelines for exploration J. Geochem. Explor., 36 (1990), pp. 445–474

White and Hedenquist, 1995 N.C. White, J.W. Hedenquist Epithermal gold deposits: styles, characteristics and exploration Soc. Econ. Geol., 23 (1995), pp. 8–13

Yumul et al., 2000 G.P. Yumul Jr., C.B. Dimalanta, H. Bellon, D.V. Faustino, J.V. De Jesus, R.A. Tamayo Jr., F.T. Jumawan Adakitic lavas in the Central Luzon back-arc region, Philippines: lower crust partial melting products? Island Arc, 9 (2000), pp. 499–512

Figures and Tables

Table 1. Composition of starting materials.

Sample	Bal 2	Pin Dac	PhM5
n	17	16	9
SiO_2 (wt.%)	65.09 (0.39)	64.45 (0.55)	63.43 (0.48)
TiO_2	0.35 (0.06)	0.50 (0.06)	0.47 (0.09)
Al_2O_3	15.60 (0.19)	15.72 (0.21)	16.32 (0.20)
Cr_2O_3	0.06 (0.06)	0.04 (0.06)	0.04 (0.03)
FeO	2.93 (0.16)	3.96 (0.20)	5.17 (0.27)
MnO	0.06 (0.06)	0.11 (0.10)	0.04 (0.06)
MgO	2.72 (0.11)	2.32 (0.08)	1.79 (0.05)
CaO	4.45 (0.10)	4.99 (0.10)	5.47 (0.12)
Na_2O	4.78 (0.09)	4.29 (0.10)	4.21 (0.13)
K_2O	1.83 (0.05)	1.54 (0.06)	0.66 (0.03)
Total	97.86 (0.44)	97.94 (0.58)	97.60 (0.50)
Sr/Y	197.8	42.4	20.8
Au (ppb)	38	12	29
S (ppm)	bdl	bdl	bdl

Major elements and sulfur in anhydrous double-melting quenched glasses (starting materials; see text) were measured by EPMA in Taipei, Taiwan (IES, Academia Sinica). Oxides and totals are in wt.%, with uncertainties presented as once the standard error of the mean ($\pm 1\sigma$) for the n replicate measurements. Bulk Au concentrations (in ppb) in natural samples were determined by ICP-MS in Toulouse, France, using the methods described by Aries et al. (2000). Sr/Y ratios of bulk natural samples (from Jégo et al. (2010)) give information about the adakitic imprint of the starting materials. bdl: below detection limit (here, <30 ppm); see text for details.

Table 2. Summary of experimental results.

Charges	H$_2$O glass	S glass	Au glass	LOD$_{min-max}$ (n)	log X_{Au}	log X_{FeS}	log X_{FeO}	aH$_2$O	log fH$_2$O	log fO$_2$	ΔNNO	log fS$_2$	log fSO$_2$	log fH$_2$S	Phases

Run No. 1: P = 4060 bar, T = 1000 °C, fH$_2$ = 1.97 bar, X_{Ni} = 0.168, t = 112.5 h

Composition Pin Dac

C4A	4.91 (0.05)	308 (148)	714 (2)	4–5 (2)	−6.70	−3.21	−1.69	0.62	3.41	−8.26	2.00	2.69	4.17	2.74	Gl (>95); Cpx (<3); Pyrrh (2); Vap
C5A	3.94 (0.12)	256 (154)	253 (36)	152–178 (3)	−7.14	−3.29	−1.69	0.48	3.30	−8.49	1.77	2.25	3.71	2.53	Gl (<95); Cpx (>3); Pyrrh (2); Au-nuggets; Vap

Run No. 3: P = 3975 bar, T = 998 °C, fH$_2$ = 4.32 bar, X_{Ni} = 0.266, t = 115 h

Composition Pin Dac

C1C	6.75 (0.06)	755 (116)	2408 (234)	4–5 (3)	−6.20	−2.82	−1.57	0.88	3.55	−8.70	1.59	*2.75*	3.76	3.13	Gl (99); Pyrrh (1); Vap
C2C	4.80 (0.05)	322 (88)	865 (32)	5–55 (5)	−6.62	−3.19	−1.71	0.61	3.39	−9.02	1.27	2.60	3.37	3.06	Gl (96); Cpx (2); Pyrrh (2); Au-nuggets; Vap
C3C	5.14 (0.20)	397 (96)	1076 (278)	5–17 (9)	−6.53	−3.10	−1.63	0.67	3.43	−8.93	1.35	3.11	3.70	3.31	Gl (98); Cpx (1); Pyrrh (1); Au-nuggets; Vap

Composition Bal2

C4C	6.59 (0.11)	553 (124)	1421 (208)	3–5 (3)	−6.43	−2.96	−1.58	0.86	3.54	−8.72	1.57	*3.00*	3.86	3.26	Gl (<100); Pyrrh; Vap
C5C	6.18 (0.16)	496 (164)	1197 (242)	4–15 (5)	−6.50	−3.00	−1.68	0.80	3.51	−8.78	1.51	2.88	3.74	3.20	Gl (97); Cpx (2); Pyrrh (1); Au-nuggets; Vap
C6C	5.81 (0.38)	482 (228)	1277 (758)	4–14 (8)	−6.46	−3.02	−1.70	0.76	3.49	−8.82	1.46	3.16	3.84	3.34	Gl (<97); Cpx (<3); Pyrrh (1); Au-nuggets; Vap

Composition PhM5

C7C	7.21 (0.09)	718 (106)	2507 (48)	4–5 (3)	−6.19	−2.84	−1.44	0.91	3.57	−8.67	1.62	2.50	3.66	3.01	Gl (99); Pyrrh (1); Vap
C8C	6.71 (0.21)	572 (92)	2009 (170)	4–7 (3)	−6.28	−2.94	−1.41	0.85	3.54	−8.73	1.56	2.72	3.71	3.12	Gl (99); Pyrrh (1); Vap
C9C	5.82 (0.14)	455 (110)	1469 (172)	4–10 (3)	−6.40	−3.04	−1.44	0.74	3.48	−8.85	1.44	2.50	3.48	3.01	Gl (99); Pyrrh (1); Vap

Run No. 4: P = 4100 bar, T = 995 °C, fH$_2$ = 0.36 bar, X_{Ni} = 0.0521, t = 100 h

Composition Pin Dac

C1D	4.78 (0.35)	2096 (108)	512 (260)	70–118 (10)	−6.85	−2.38	−1.46	0.57	3.38	−6.94	3.39	*−3.50*	2.39	−1.04	Gl (98); Anhd (2); Mgt; Au-nuggets; Vap
C2D	3.76 (0.11)	1892 (116)	466 (280)	78–200 (8)	−6.87	−2.42	−1.49	0.44	3.27	−7.17	3.16	*−3.00*	2.41	−0.79	Gl (97); Anhd (>2); Mgt (<1); Au-nuggets; Vap
C3D	3.44 (0.23)	1651 (140)	462 (184)	90–236 (10)	−6.87	−2.48	−1.45	0.37	3.19	−7.32	3.01	−2.50	2.51	−0.54	Gl (98); Anhd (2); Mgt; Au-nuggets; Vap

Composition Bal2

C4D	5.59 (0.13)	2422 (146)	537 (214)	82–173 (6)	−6.84	−2.32	−1.57	0.63	3.42	−6.86	3.47	*−3.50*	2.47	−1.04	Gl (>98); Anhd (<2); Mgt; Au-nuggets; Vap
C5D	4.44 (0.08)	2184 (170)	682 (214)	96–169 (7)	−6.72	−2.36	−1.57	0.49	3.31	−7.07	3.26	*−3.25*	2.38	−0.92	Gl (98); Anhd (2); Mgt; Au-nuggets; Vap
C6D	3.46 (0.30)	1795 (222)	657 (572)	87–162 (6)	−6.72	−2.44	−1.61	0.36	3.18	−7.34	2.99	−2.50	2.49	−0.54	Gl (97); Opx (1); Anhd (2); Mgt; Au-nuggets; Vap

Composition PhM5

C7D	5.27 (0.31)	1851 (138)	521 (160)	88–167 (6)	−6.84	−2.43	−1.42	0.69	3.46	−6.78	3.55	−3.76	2.42	−1.17	Gl (>96); Anhd (>2); Mgt (>1); Au-nuggets; Vap
C8D	4.67 (0.33)	1619 (132)	724 (256)	65–149 (5)	−6.69	−2.49	−1.43	0.59	3.39	−6.91	3.42	−3.45	2.44	−1.02	Gl (<97); Anhd (2); Mgt (>1); Au-nuggets;

Charges	H$_2$O glass	S glass	Au glass	LOD$_{min-max}$ (n)	log X_{Au}	log X_{FeS}	log X_{FeO}	aH$_2$O	log fH$_2$O	log fO$_2$	ΔNNO	log fS$_2$	log fSO$_2$	log fH$_2$S	Phases
															Vap
C9D	3.96 (0.03)	1400 (128)	633	122 (1)	−6.74	−2.55	−1.42	0.48	3.30	−7.09	3.24	−3.03	2.47	−0.81	Gl (97); Anhd (2); Mgt (1); Au-nuggets; Vap

Run No. 5: P = 4110 bar, T = 995 °C, fH$_2$ = 91.38 bar, X_{Co} = 0.455, t = 116 h

Composition Pin Dac

Charges	H$_2$O glass	S glass	Au glass	LOD$_{min-max}$ (n)	log X_{Au}	log X_{FeS}	log X_{FeO}	aH$_2$O	log fH$_2$O	log fO$_2$	ΔNNO	log fS$_2$	log fSO$_2$	log fH$_2$S	Phases
C1E	8.03 (1.04)	957 (1626)	4253 (356)	8–8 (4)	−5.97	−2.72	−1.91	0.99	3.62	−11.26	−0.93	2.13	0.88	4.17	Gl (>97); Pyrrh (<3); Vap
C2E	6.19 (0.42)	570 (188)	1686 (312)	6–8 (4)	−6.35	−2.94	−1.56	0.79	3.52	−11.46	−1.13	1.15	0.20	3.68	Gl (>99); Pyrrh (<1); Au-nuggets; Vap
C3E	5.86 (0.16)	548 (116)	1209 (228)	6–22 (6)	−6.49	−2.96	−1.73	0.74	3.49	−11.52	−1.19	*1.00*	0.07	3.61	Gl (98); Pyrrh (2); Vap

Composition Bal2

Charges	H$_2$O glass	S glass	Au glass	LOD$_{min-max}$ (n)	log X_{Au}	log X_{FeS}	log X_{FeO}	aH$_2$O	log fH$_2$O	log fO$_2$	ΔNNO	log fS$_2$	log fSO$_2$	log fH$_2$S	Phases
C4E	7.25 (0.30)	597 (330)	1982 (484)	5–8 (4)	−6.29	−2.92	−1.76	0.91	3.58	−11.34	−1.01	*1.25*	0.37	3.73	Gl (<99); Pyrrh (>1); Vap
C5E	6.91 (0.25)	604 (444)	2342 (162)	6–16 (5)	−6.21	−2.92	−1.75	0.87	3.56	−11.37	−1.05	*1.25*	0.33	3.73	Gl (<99); Pyrrh (>1); Au-nuggets; Vap
C6E	5.82 (0.33)	1752 (1308)	1159 (164)	6–24 (7)	−6.51	−2.46	−1.75	0.75	3.50	−11.50	−1.17	*1.25*	0.20	3.73	Gl (99); Pyrrh (1); Au-nuggets; Vap

Composition PhM5

Charges	H$_2$O glass	S glass	Au glass	LOD$_{min-max}$ (n)	log X_{Au}	log X_{FeS}	log X_{FeO}	aH$_2$O	log fH$_2$O	log fO$_2$	ΔNNO	log fS$_2$	log fSO$_2$	log fH$_2$S	Phases
C7E	7.51 (0.37)	1110 (1544)	1993 (148)	5–7 (4)	−6.29	−2.65	−1.69	0.90	3.58	−11.35	−1.02	1.61	0.54	3.91	Gl (97); Pyrrh (3); Vap
C8E	7.94 (0.20)	837 (458)	2020 (54)	5–6 (4)	−6.29	−2.77	−1.67	0.95	3.60	−11.30	−0.97	1.28	0.42	3.75	Gl (97); Pyrrh (3); Vap
C9E	6.18 (0.16)	1498 (308)	1054 (166)	8–43 (8)	−6.55	−2.52	−1.62	0.75	3.50	−11.50	−1.17	0.52	−0.16	3.37	Gl (>97); Pyrrh (<3); Au-nuggets; Vap

Run No. 6: P = 3950 bar, T = 1000 °C, fH$_2$ = 93.68 bar, X_{Co} = 0.471, t = 136 h

Composition Pin Dac

Charges	H$_2$O glass	S glass	Au glass	LOD$_{min-max}$ (n)	log X_{Au}	log X_{FeS}	log X_{FeO}	aH$_2$O	log fH$_2$O	log fO$_2$	ΔNNO	log fS$_2$	log fSO$_2$	log fH$_2$S	Phases
C1F	8.03 (0.98)	739 (90)	2506 (82)	5–6 (3)	−6.20	−2.83	−2.14	1.00	3.60	−11.23	−0.97	2.28	0.99	4.22	Gl (97); Pyrrh (3); Vap
C2F	7.31 (0.70)	702 (128)	2147 (170)	7–21 (3)	−6.26	−2.85	−2.14	0.92	3.57	−11.30	−1.05	1.88	0.72	4.02	Gl (97); Pyrrh (3); Au-nuggets; Vap
C3F	7.70 (1.10)	712 (96)	2086 (222)	9–41 (6)	−6.27	−2.85	−2.18	0.97	3.59	−11.26	−1.00	1.82	0.73	3.99	Gl (>96); Cpx (<1); Pyrrh (3); Vap

Composition Bal2

Charges	H$_2$O glass	S glass	Au glass	LOD$_{min-max}$ (n)	log X_{Au}	log X_{FeS}	log X_{FeO}	aH$_2$O	log fH$_2$O	log fO$_2$	ΔNNO	log fS$_2$	log fSO$_2$	log fH$_2$S	Phases
C4F	7.72 (0.08)	794 (90)	2700 (170)	7–32 (4)	−6.16	−2.80	−2.16	0.97	3.59	−11.26	−1.00	2.27	0.96	4.21	Gl (>95); Cpx (2); Pyrrh (>2); Vap
C5F	7.60 (0.01)	880 (100)	3395 (846)	5–10 (3)	−6.06	−2.75	−2.22	0.95	3.58	−11.27	−1.02	2.66	1.14	4.41	Gl (<95); Cpx (<3); Pyrrh (>2); Vap
C6F	6.80 (0.08)	624 (100)	1673 (232)	6–102 (9)	−6.36	−2.90	−2.19	0.87	3.54	−11.35	−1.09	2.42	0.94	4.29	Gl (97); Pyrrh (3); Au-nuggets; Vap

Composition PhM5

Charges	H$_2$O glass	S glass	Au glass	LOD$_{min-max}$ (n)	log X_{Au}	log X_{FeS}	log X_{FeO}	aH$_2$O	log fH$_2$O	log fO$_2$	ΔNNO	log fS$_2$	log fSO$_2$	log fH$_2$S	Phases
C7F	7.72 (0.04)	1046 (118)	4064 (280)	10–48 (8)	−5.98	−2.68	−2.38	0.94	3.58	−11.28	−1.03	2.79	1.19	4.47	Gl (>95); Pyrrh (<5); Au-nuggets; Vap
C8F	6.83 (0.12)	1202 (98)	5159 (144)	6–16 (4)	−5.87	−2.62	−2.65	0.83	3.52	−11.39	−1.13	2.93	1.15	4.54	Gl (>95); Pyrrh (<5); Vap
C9F	7.22 (0.08)	1067 (114)	4234 (312)	9–32 (8)	−5.96	−2.67	−2.52	0.87	3.54	−11.31	−1.09	3.00	1.27	4.56	Gl (>95); Pyrrh (<5); Au-nuggets; Vap

H$_2$O glass in wt.% ($\pm 1\sigma$); S glass in ppm ($\pm 2\sigma$); $X\mathrm{SO}_4^{2-}/X\mathrm{S}_{\mathrm{tot}}$: proportion of sulfur dissolved as sulfate species (SO_4^{2-}) in melt (calculations from the calibration of Matthews et al., 1999). Au glass in ppb ($\pm 2\sigma$). LOD: limit of detection (in ppb) for Au glass; n is the number of Au glass analyses per charge. Note that the LODmin (LODmax) is not necessarily relative to the lowest (highest) melt gold content measured in the charge; LOD is mainly controlled by the width of the signal part used for calculations (see Jégo et al., 2010). log X_{Au}: logarithm of the gold mole fraction in the experimental silicate glass. X_{Ni} (runs 1, 3, 4) and X_{Co} (runs 5, 6) are the average proportions of Ni and Co, respectively, in solid sensor alloys (see text for details). t is the experimental duration in hours. fH$_2$ values are calculated from the fO$_2$ in the sensor capsule (Taylor et al., 1992), taking fH$_2$O = fH$_2$O. ΔNNO: log fO$_2$ of the charge $-$ log fO$_2$ of the NNO equilibrium at the same pressure and temperature. log fS$_2$ in reduced/moderately oxidized charges was calculated from the composition of pyrrhotite (Froese and Gunter, 1976). log fS$_2$ in highly oxidized charges was determined from the assemblage anhydrite + magnetite, using MELTS for calculation of the component activities. log fSO$_2$ and log fH$_2$S were obtained by using the equilibrium constants of Ohmoto and Kerrick (1977). Gl, glass; Pyrrh, pyrrhotite; Cpx, clinopyroxene; Opx, orthopyroxene; Anhd, anhydrite; Vap, vapour phase; Au-nuggets, gold micro-crystals. A vapour phase is systematically indicated for all charges (see text for explanations). Phase proportions (in wt.%) were estimated by mass-balance calculations. Note that the log fS$_2$ values in italics refer to charges where pyrrhotite or magnetite crystals were not large enough to be satisfactorily analyzed by EPMA; therefore, the corresponding fS$_2$ values were estimated by comparison with the fS$_2$ calculated for the other charges, considering other variables such as melt composition, melt S content and fO$_2$. In addition, as pointed out in the text, run 6 is a duplicate of run 5 whose the quench was slower than intended, inducing the formation of abundant micro-bubbles and resulting in a significant heterogeneity of sulfur concentrations in melt.
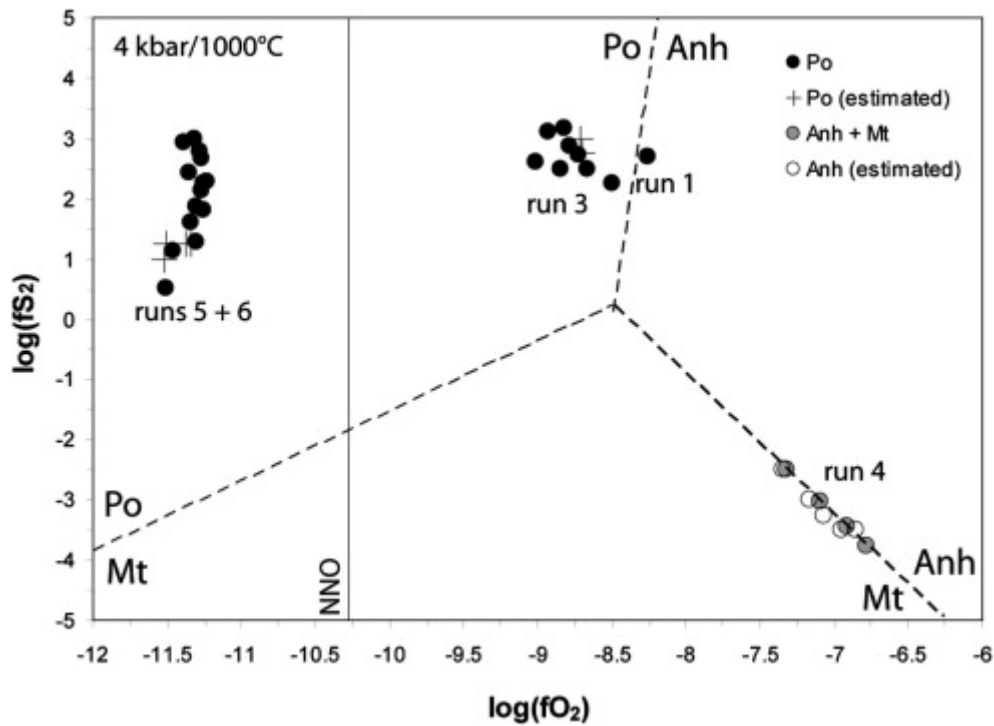
Fig. 1. Sulfur fugacity (log fS_2) of the experimental charges as a function of their oxygen fugacity (log fO_2). Calculations of fS_2 and fO_2 values are explained in the text (Section 3.4.4). Stability field boundaries for pyrrhotite (Po), anhydrite (Anh) and magnetite (Mt) at 0.4 GPa and 1000 °C were calculated from mineral–melt equilibria (see Appendix). Charges are separated on the basis of their sulfur-bearing phase assemblage (either Po or Anh + Mt). Sulfur fugacities of charges with crystals (either Po or Mt) too small for analysis have been estimated by using the other charges (see text, Section 4.1, and Table 2).
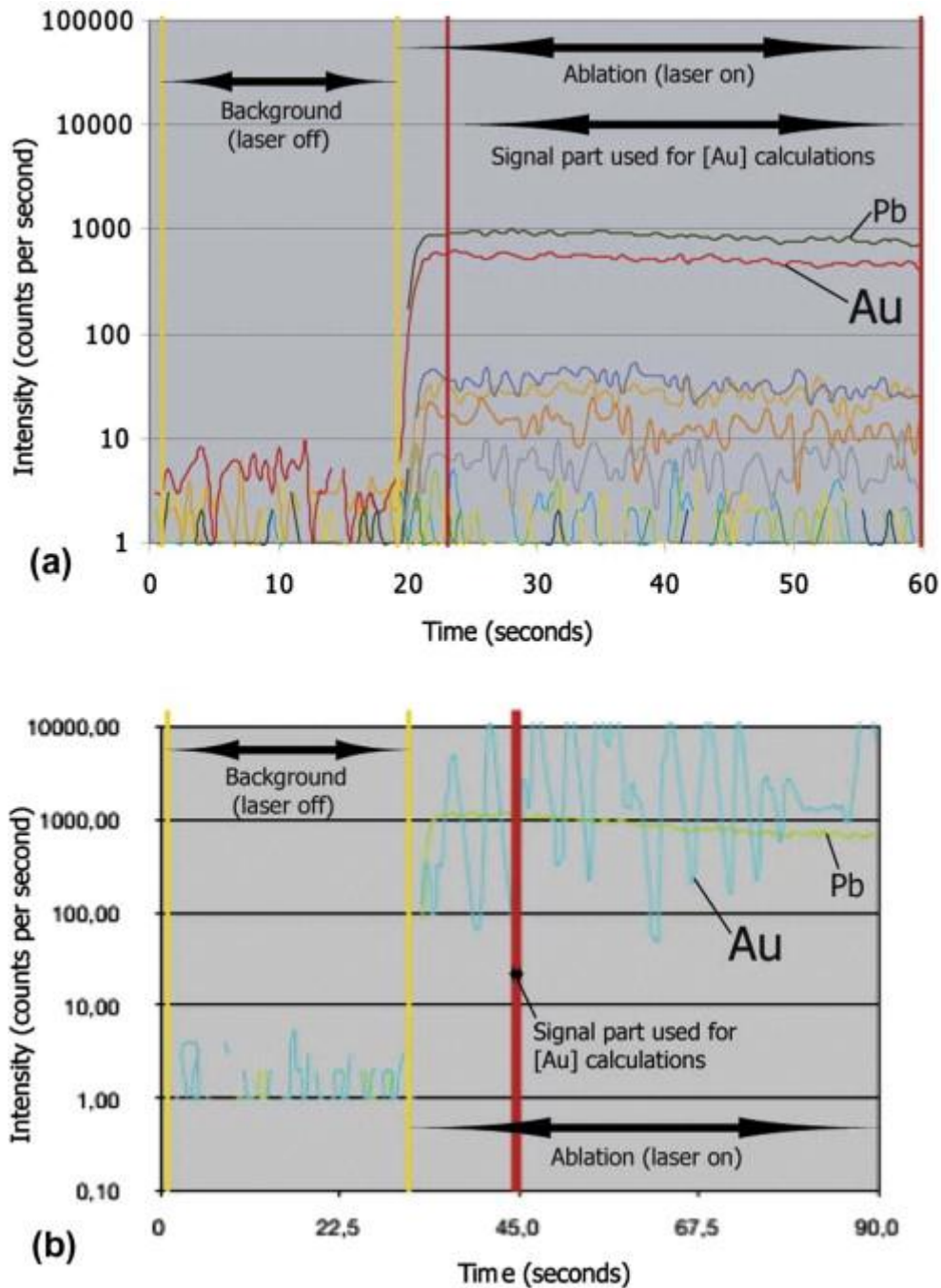
Fig. 2. (a) Example of a typical ablation signal on a silicate glass. Records of counts (in logarithmic scale) are plotted vs. time (in seconds). The yellow vertical border lines delimit the background signal part before ablation (needed for concentrations calculations), whereas the red ones define the actual ablation signal part. The laser is turned on after about 20 s of background. In this example, gold (in red) and lead (in black) ablation signal curves are high and flat, allowing easy determination of Au and Pb glass contents by considering the whole ablation part. The other ablation signal curves are relative to ultra-trace elements (e.g. platinum-group elements), whose contents are below the detection limit of the analytical equipment; their very low and noisy signals can not be used for determining correct glass contents. (b) Example of ablation signal from run 4 displaying unwanted peaks related to Au-nuggets. In this case, the red vertical border lines are manually brought closer to each other and moved on the widest flat portion of the gold ablation part (which here is very narrow) in order to avoid peaks related to gold particles and get a correct signal for the determination of Au contents. Note that the detection limit is increased by bringing the red border lines closer to each other.

Table 5. Compositions of experimental pyrrhotites and estimates of $f\mathrm{S}_2$.

Charge	C4A	C5A	C2C	C3C	C5C	C6C	C7C	C8C
n	11	8	15	3	8	6	10	7
Fe	57.81 (0.49)	58.47 (0.47)	58.06 (0.60)	58.55 (0.55)	57.94 (0.76)	57.31 (0.57)	58.70 (0.42)	58.07 (0.58)
S	40.66 (0.31)	40.29 (0.45)	40.69 (0.46)	42.13 (0.11)	41.19 (0.54)	41.36 (0.56)	40.94 (0.47)	40.95 (0.52)
O	0.47 (0.33)	0.12 (0.35)	0.11 (0.26)	0.41 (0.12)	0.42 (0.25)	0.46 (0.32)	0.30 (0.14)	0.52 (0.26)
Total	98.95 (0.30)	98.87 (0.17)	98.86 (0.37)	101.09 (0.41)	99.55 (0.82)	99.12 (0.41)	99.94 (0.68)	99.53 (0.67)
NFeS	0.899	0.909	0.901	0.888	0.894	0.886	0.903	0.898
X_{FeS}	0.816	0.833	0.819	0.798	0.808	0.796	0.823	0.814
$\log f\mathrm{S}_2$	2.69	2.25	2.60	3.11	2.88	3.16	2.50	2.72

	C9C	C1E	C2E	C7E	C8E	C9E	C1F	C2F
n	9	6	5	4	6	6	12	5
Fe	58.60 (0.38)	58.73 (0.82)	59.67 (0.29)	60.28 (0.43)	60.22 (0.60)	59.64 (1.22)	58.90 (0.46)	60.29 (0.48)
S	40.87 (0.38)	40.28 (0.60)	39.37 (0.26)	40.47 (0.12)	39.92 (0.79)	38.51 (1.61)	40.66 (1.09)	40.90 (0.38)
O	0.32 (0.20)	0.87 (0.08)	0.04 (0.05)	0.02 (0.05)	0.04 (0.05)	0.14 (0.23)	0.25 (0.25)	0.03 (0.05)
Total	99.79 (0.47)	99.89 (0.86)	99.09 (0.37)	100.78 (0.53)	100.17 (1.03)	98.28 (2.54)	99.81 (0.89)	101.22 (0.62)
NFeS	0.903	0.911	0.931	0.922	0.928	0.941	0.908	0.917
X_{FeS}	0.823	0.837	0.870	0.855	0.866	0.889	0.832	0.846
$\log f\mathrm{S}_2$	2.50	2.13	1.15	1.61	1.28	0.52	2.28	1.88

	C3F	C4F	C5F	C6F	C7F	C8F	C9F
n	5	8	10	13	16	12	13
Fe	60.18 (0.35)	57.56 (0.46)	57.23 (0.54)	57.67 (0.51)	57.58 (0.68)	58.00 (0.82)	57.45 (0.29)
S	40.73 (0.21)	39.72 (0.37)	40.23 (0.32)	40.06 (0.31)	40.73 (0.19)	41.33 (0.24)	41.08 (0.31)
O	0.05 (0.07)	0.07 (0.05)	0.18 (0.19)	0.17 (0.18)	0.18 (0.20)	0.05 (0.06)	0.16 (0.09)
Total	100.96 (0.27)	97.37 (0.22)	97.63 (0.50)	97.89 (0.49)	98.50 (0.66)	99.46 (0.85)	98.68 (0.39)
NFeS	0.918	0.908	0.899	0.905	0.896	0.892	0.891
X_{FeS}	0.848	0.832	0.817	0.827	0.812	0.806	0.803
$\log f\mathrm{S}_2$	1.82	2.27	2.66	2.42	2.79	2.93	3.00

Concentrations of Fe, S, and O are in wt.%, with uncertainties presented as once the standard error of the mean ($\pm 1\sigma$) for the n replicate measurements. Mole fractions of FeS in FeS–S_2 and FeS–S systems, respectively N_{FeS} and X_{FeS}, as well as the method of calculation of $\log f\mathrm{S}_2$ from X_{FeS}, are taken from Froese and Gunter (1976)
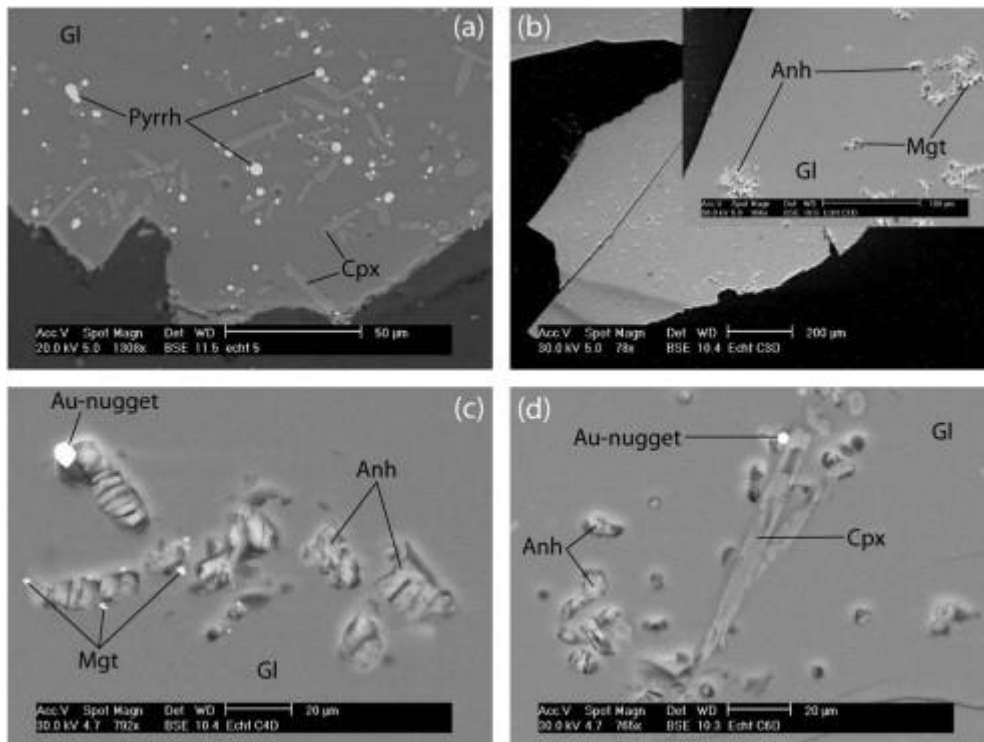
Fig. 3. Back-scattered electron (BSE) pictures of representative experimental charges. (a) Phase assemblage and texture typical of reduced and moderately oxidizing charges (runs 1, 3, 5, 6). Note that most sulfides are spatially associated to pyroxene crystals. (b) Phase assemblage and texture typical of highly oxidized charges (run 4). Magnetite crystals are intimately enclosed in anhydrite clusters. (c) Detail of the charge C4D showing a large Au-nugget (>5 μm) and many tiny magnetites (<1 μm) in close textural association with anhydrite crystal and bubble. (d) Detail of the charge C6D showing a gold-nugget (<5 μm) at the interface between Cpx, Anh and silicate melt. Gl, melt quenched to glass; Cpx, clinopyroxene; Pyrrh, pyrrhotite; Anh, anhydrite; Mgt, magnetite.

Table 3. Compositions of experimental pyroxenes.

Charge	C4A	C5A	C2C	C3C	C5C	C6C	C3F	C4F	C5F	C6D
Phases	Clinopyroxenes									Orthopyroxenes
n	19	15	26	2	12	18	1	13	5	10
SiO_2	53.23 (1.16)	53.34 (1.10)	53.06 (0.70)	53.35 (0.38)	53.63 (0.54)	53.55 (0.42)	52.94	53.01 (0.50)	53.73 (0.35)	55.89 (0.79)
Al_2O_3	2.99 (1.05)	3.24 (0.98)	2.37 (0.84)	2.13 (0.32)	1.65 (0.31)	1.78 (0.19)	1.08	1.65 (0.38)	1.35 (0.39)	2.08 (0.54)
K_2O	0.07 (0.06)	0.10 (0.11)	0.05 (0.07)	0.00 (0.00)	0.03 (0.02)	0.03 (0.03)	0.00	0.03 (0.02)	0.02 (0.03)	0.02 (0.02)
Na_2O	0.44 (0.11)	0.52 (0.22)	0.32 (0.13)	0.36 (0.05)	0.38 (0.10)	0.39 (0.05)	0.21	0.38 (0.09)	0.30 (0.08)	0.06 (0.05)
CaO	20.30 (0.97)	19.23 (0.96)	20.27 (1.46)	22.08 (0.00)	21.07 (1.15)	20.78 (0.68)	22.57	22.75 (0.53)	22.41 (0.67)	1.42 (0.39)
FeO	4.09 (1.05)	5.24 (0.63)	3.67 (0.67)	2.28 (0.83)	1.90 (0.37)	2.56 (0.52)	1.14	1.33 (0.30)	0.78 (0.31)	5.74 (1.40)
MnO	0.27 (0.11)	0.39 (0.13)	0.36 (0.10)	0.25 (0.08)	0.14 (0.10)	0.13 (0.08)	0.13	0.10 (0.08)	0.07 (0.06)	0.16 (0.12)
MgO	16.57 (1.17)	15.93 (0.97)	17.90 (1.48)	18.15 (0.57)	18.62 (1.02)	18.03 (0.58)	21.01	19.57 (0.68)	20.55 (0.41)	32.13 (0.88)
TiO_2	0.40 (0.14)	0.47 (0.12)	0.34 (0.10)	0.47 (0.12)	0.19 (0.08)	0.21 (0.07)	0.24	0.24 (0.07)	0.18 (0.08)	0.13 (0.05)
Cr_2O_3	0.19 (0.08)	0.16 (0.12)	0.34 (0.19)	0.34 (0.06)	0.97 (0.32)	0.92 (0.30)	n.a.	n.a.	n.a.	0.78 (0.28)
Total	98.57 (0.43)	98.63 (0.32)	98.68 (0.43)	99.41 (0.01)	98.57 (0.31)	98.40 (0.25)	99.32	99.07 (0.57)	99.40 (0.49)	98.40 (0.33)
Wo%	41.97	39.87	41.70	45.22	43.18	42.67	46.22	47.14	45.56	2.72
En%	47.65	45.94	51.23	51.72	53.07	51.50	59.89	56.41	58.15	85.88
Fs%	10.38	14.19	7.07	3.07	3.75	5.83	−6.11	−3.54	−3.71	11.40
Mg#	82.76	77.23	88.76	95.11	93.77	90.17	111.79	107.03	107.03	88.51

Oxides and totals are in wt.%, with uncertainties presented as once the standard error of the mean ($\pm 1\sigma$) for the *n* replicate measurements. For each charge, the proportions of pure wollastonite (Wo), enstatite (En) and ferrosillite (Fs) were calculated from the structural formula of the average pyroxene (considering FeO = FeO total), together with the corresponding Mg# (= 100 * [Mg]/([Mg] + [Fe])). n.a., not analyzed.

Table 4. Compositions of experimental Fe-oxides from run 4.

Charge	C3D	C7D	C8D	C9D
n	5	7	5	5
SiO_2	0.29 (0.22)	0.08 (0.06)	0.11 (0.03)	0.08 (0.06)
Al_2O_3	6.20 (0.45)	6.36 (0.17)	7.27 (0.29)	7.42 (0.16)
K_2O	0.03 (0.01)	0.01 (0.02)	0.02 (0.02)	0.02 (0.02)
Na_2O	0.00 (0.01)	0.01 (0.02)	0.02 (0.03)	0.01 (0.02)
CaO	0.17 (0.08)	0.19 (0.11)	0.11 (0.11)	0.07 (0.06)
FeO	73.17 (0.93)	78.51 (0.89)	78.13 (1.18)	77.49 (1.16)
MnO	0.40 (0.08)	0.20 (0.06)	0.15 (0.11)	0.13 (0.10)
MgO	5.78 (0.29)	4.30 (0.35)	4.52 (0.21)	4.45 (0.11)
TiO_2	1.07 (0.07)	0.77 (0.05)	0.94 (0.08)	0.95 (0.06)
Cr_2O_3	2.39 (0.45)	0.16 (0.09)	0.08 (0.06)	0.14 (0.08)
Total	89.50 (1.29)	90.59 (0.94)	91.34 (0.93)	90.77 (1.35)

Oxides and totals are in wt.%, with uncertainties presented as once the standard error of the mean ($\pm 1\sigma$) for the *n* replicate measurements. All 'run 4' charges contain magnetite, but only these four ones display crystals large enough to be correctly analyzed.

Table 6. Concentrations of major elements (EPMA data) in the run product glasses of S-added charges.

Charge	C4A	C5A	C1C	C2C	C3C	C4C	C5C	C6C	C7C	C8C
n	15	15	11	14	15	12	12	13	12	11
SiO_2	67.45 (0.72)	67.52 (0.52)	66.74 (0.98)	67.30 (0.66)	66.92 (1.15)	66.78 (0.98)	67.40 (0.89)	67.51 (1.13)	66.01 (1.15)	65.78 (0.77)
Al_2O_3	16.57 (0.39)	16.73 (0.31)	16.19 (0.27)	16.67 (0.31)	16.30 (0.32)	16.02 (0.44)	16.37 (0.28)	16.41 (0.28)	16.87 (0.37)	16.80 (0.24)
K_2O	1.63 (0.12)	1.67 (0.12)	1.60 (0.15)	1.72 (0.16)	1.67 (0.12)	1.91 (0.16)	1.91 (0.14)	1.98 (0.15)	0.69 (0.09)	0.67 (0.11)
Na_2O	4.96 (0.20)	4.91 (0.23)	4.48 (0.23)	4.73 (0.22)	4.69 (0.25)	5.07 (0.16)	5.09 (0.25)	5.19 (0.26)	4.42 (0.20)	4.51 (0.25)
CaO	4.58 (0.27)	4.53 (0.35)	5.01 (0.30)	4.72 (0.30)	4.89 (0.28)	4.29 (0.27)	4.09 (0.31)	4.00 (0.18)	5.56 (0.29)	5.54 (0.24)
FeO	2.26 (0.81)	2.29 (0.47)	2.99 (0.36)	2.20 (0.31)	2.65 (0.30)	2.98 (0.42)	2.36 (0.35)	2.23 (0.33)	4.06 (0.41)	4.37 (0.41)
MnO	0.10 (0.14)	0.06 (0.09)	0.12 (0.16)	0.08 (0.14)	0.12 (0.14)	0.03 (0.06)	0.06 (0.14)	0.07 (0.14)	0.07 (0.16)	0.08 (0.17)
MgO	1.88 (0.14)	1.74 (0.12)	2.32 (0.14)	2.01 (0.14)	2.20 (0.16)	2.57 (0.18)	2.32 (0.18)	2.26 (0.14)	1.79 (0.11)	1.75 (0.10)
TiO_2	0.54 (0.12)	0.52 (0.13)	0.52 (0.16)	0.56 (0.10)	0.54 (0.10)	0.35 (0.11)	0.37 (0.09)	0.33 (0.11)	0.51 (0.08)	0.47 (0.12)
Cr_2O_3	0.03 (0.06)	0.04 (0.09)	0.05 (0.11)	0.02 (0.05)	0.03 (0.13)	0.00 (0.01)	0.04 (0.10)	0.01 (0.04)	0.03 (0.09)	0.03 (0.06)
Total	93.32 (1.36)	94.27 (0.94)	90.60 (1.18)	92.88 (0.86)	92.19 (1.32)	90.80 (1.55)	91.09 (1.08)	91.53 (1.34)	89.94 (1.37)	90.76 (0.80)

	C9C	C1D	C2D	C3D	C4D	C5D	C6D	C7D	C8D	C9D
n	12	12	14	15	14	12	12	12	13	14
SiO_2	65.93 (0.99)	67.62 (1.07)	68.02 (1.11)	67.18 (1.01)	67.72 (0.99)	67.94 (0.95)	68.12 (1.25)	67.65 (0.83)	67.61 (1.01)	67.21 (0.91)
Al_2O_3	16.87 (0.58)	16.44 (0.23)	16.55 (0.29)	16.30 (0.46)	16.07 (0.35)	16.19 (0.49)	16.44 (0.23)	17.19 (0.38)	17.10 (0.39)	17.11 (0.48)
K_2O	0.69 (0.10)	1.64 (0.20)	1.70 (0.12)	1.60 (0.13)	1.93 (0.11)	1.95 (0.16)	1.98 (0.14)	0.67 (0.12)	0.67 (0.07)	0.69 (0.11)
Na_2O	4.49 (0.29)	4.61 (0.22)	4.68 (0.24)	4.58 (0.24)	5.07 (0.27)	5.11 (0.29)	5.25 (0.23)	4.59 (0.17)	4.67 (0.28)	4.63 (0.17)
CaO	5.55 (0.40)	2.98 (0.30)	2.55 (0.27)	3.28 (0.21)	3.03 (0.21)	2.63 (0.13)	2.58 (0.25)	3.36 (0.23)	3.52 (0.23)	3.78 (0.34)
FeO	4.07 (0.38)	3.84 (0.53)	3.60 (0.43)	3.97 (0.52)	3.05 (0.32)	3.05 (0.39)	2.75 (0.52)	4.20 (0.50)	4.18 (0.39)	4.27 (0.54)
MnO	0.11 (0.19)	0.04 (0.09)	0.08 (0.14)	0.11 (0.14)	0.07 (0.16)	0.06 (0.13)	0.07 (0.12)	0.08 (0.15)	0.06 (0.10)	0.02 (0.07)
MgO	1.75 (0.14)	2.28 (0.15)	2.26 (0.14)	2.42 (0.10)	2.66 (0.14)	2.72 (0.19)	2.42 (0.15)	1.73 (0.11)	1.70 (0.12)	1.74 (0.11)
TiO_2	0.51 (0.07)	0.53 (0.13)	0.55 (0.07)	0.54 (0.09)	0.37 (0.14)	0.33 (0.17)	0.36 (0.09)	0.51 (0.11)	0.48 (0.11)	0.53 (0.11)
Cr_2O_3	0.04 (0.11)	0.02 (0.05)	0.02 (0.07)	0.03 (0.09)	0.02 (0.08)	0.03 (0.09)	0.03 (0.09)	0.01 (0.03)	0.02 (0.06)	0.02 (0.05)
Total	91.97 (1.16)	91.55 (1.24)	92.51 (1.02)	93.12 (1.17)	91.20 (1.37)	92.62 (1.39)	93.49 (1.63)	91.65 (0.97)	92.57 (1.16)	92.90 (1.65)

	C1E	C2E	C3E	C4E	C5E	C6E	C7E	C8E	C9E

Charge	C4A	C5A	C1C	C2C	C3C	C4C	C5C	C6C	C7C	C8C
n	12	12	11	11	12	11	13	11	11	
SiO_2	68.24 (1.85)	66.35 (0.70)	66.86 (0.87)	67.38 (0.80)	67.42 (1.24)	66.95 (0.79)	67.21 (0.95)	66.93 (0.99)	66.58 (0.83)	
Al_2O_3	16.76 (0.81)	16.34 (0.43)	16.63 (0.49)	16.37 (0.47)	16.36 (0.31)	16.18 (0.30)	17.37 (0.38)	17.41 (0.35)	17.23 (0.48)	
K_2O	1.65 (0.17)	1.54 (0.21)	1.66 (0.11)	1.92 (0.22)	1.89 (0.21)	1.95 (0.18)	0.70 (0.19)	0.71 (0.08)	0.69 (0.10)	
Na_2O	4.48 (0.39)	4.58 (0.32)	4.65 (0.16)	5.03 (0.23)	5.02 (0.26)	5.14 (0.32)	4.32 (0.42)	4.49 (0.30)	4.69 (0.18)	
CaO	5.50 (0.78)	5.43 (0.31)	5.16 (0.31)	4.64 (0.58)	4.70 (0.52)	4.62 (0.23)	6.09 (0.55)	6.17 (0.40)	5.75 (0.28)	
FeO	1.38 (0.72)	3.1 (0.68)	2.07 (0.24)	1.93 (0.38)	1.97 (0.49)	2.00 (0.30)	2.29 (1.51)	2.39 (0.46)	2.66 (0.31)	
MnO	0.13 (0.11)	0.08 (0.13)	0.14 (0.21)	0.02 (0.06)	0.07 (0.12)	0.08 (0.14)	0.10 (0.18)	0.10 (0.14)	0.07 (0.11)	
MgO	1.31 (1.02)	2.01 (0.44)	2.3 (0.29)	2.33 (0.75)	2.21 (0.62)	2.70 (0.29)	1.39 (0.56)	1.25 (0.38)	1.79 (0.12)	
TiO_2	0.56 (0.11)	0.54 (0.13)	0.51 (0.11)	0.36 (0.08)	0.36 (0.08)	0.35 (0.09)	0.52 (0.15)	0.53 (0.16)	0.50 (0.14)	
Cr_2O_3	0.01 (0.02)	0.04 (0.09)	0.03 (0.06)	0.04 (0.13)	0.01 (0.05)	0.05 (0.15)	0.02 (0.07)	0.03 (0.08)	0.03 (0.06)	
Total	88.75 (1.66)	90.21 (1.03)	90.95 (1.02)	89.53 (1.15)	90.10 (1.36)	91.13 (1.08)	88.46 (2.47)	89.40 (1.23)	91.03 (1.09)	

	C1F	C2F	C3F	C4F	C5F	C6F	C7F	C8F	C9F
n	10	10	10	10	9	11	10	10	10
SiO_2	68.42 (0.80)	68.25 (0.64)	68.28 (1.20)	69.02 (0.83)	69.02 (0.93)	69.20 (1.42)	68.55 (0.62)	68.66 (0.57)	68.33 (1.90)
Al_2O_3	16.76 (0.32)	16.84 (0.48)	16.87 (0.34)	16.86 (0.18)	17.01 (0.39)	17.13 (0.33)	17.62 (0.38)	17.57 (0.32)	17.67 (0.53)
K_2O	1.62 (0.14)	1.63 (0.18)	1.63 (0.20)	1.92 (0.16)	1.93 (0.18)	1.98 (0.13)	0.69 (0.10)	0.70 (0.09)	0.72 (0.11)
Na_2O	3.98 (0.28)	4.02 (0.20)	4.17 (0.26)	4.20 (0.24)	4.52 (0.21)	4.45 (0.27)	4.21 (0.23)	4.33 (0.17)	4.37 (0.20)
CaO	5.12 (0.44)	5.13 (0.22)	5.09 (0.32)	4.19 (0.23)	4.08 (0.36)	3.85 (0.26)	5.83 (0.40)	5.85 (0.39)	5.93 (0.35)
FeO	0.82 (0.18)	0.82 (0.16)	0.75 (0.34)	0.78 (0.12)	0.68 (0.41)	0.73 (0.24)	0.47 (0.17)	0.25 (0.23)	0.34 (0.14)
MnO	0.11 (0.16)	0.13 (0.14)	0.14 (0.12)	0.07 (0.12)	0.02 (0.06)	0.03 (0.08)	0.07 (0.09)	0.07 (0.10)	0.06 (0.09)
MgO	2.57 (0.22)	2.59 (0.16)	2.49 (0.26)	2.55 (0.11)	2.44 (0.15)	2.26 (0.24)	1.99 (0.14)	1.98 (0.10)	1.99 (0.14)
TiO_2	0.57 (0.12)	0.55 (0.12)	0.52 (0.16)	0.39 (0.13)	0.30 (0.06)	0.37 (0.13)	0.54 (0.10)	0.54 (0.16)	0.55 (0.13)
Cr_2O_3	0.03 (0.08)	0.04 (0.10)	0.04 (0.06)	0.01 (0.03)	0.01 (0.03)	0.02 (0.06)	0.04 (0.07)	0.04 (0.10)	0.04 (0.09)
Total	90.8 (1.24)	91.03 (1.32)	91.82 (1.90)	90.86 (0.94)	91.17 (1.15)	91.75 (1.80)	92.25 (1.41)	92.48 (0.83)	92.63 (2.64)

Oxides and totals are in wt.%, with uncertainties presented as once the standard error of the mean ($\pm 1\sigma$) for the n replicate measurements. For each charge, concentrations of oxides were normalized to 100 wt.% (i.e., anhydrous) and adjusted to minimize the

effect of migration of the alkalis (Na, K) (see text). Totals are presented before normalization; they are thus relative to the hydrous glasses.
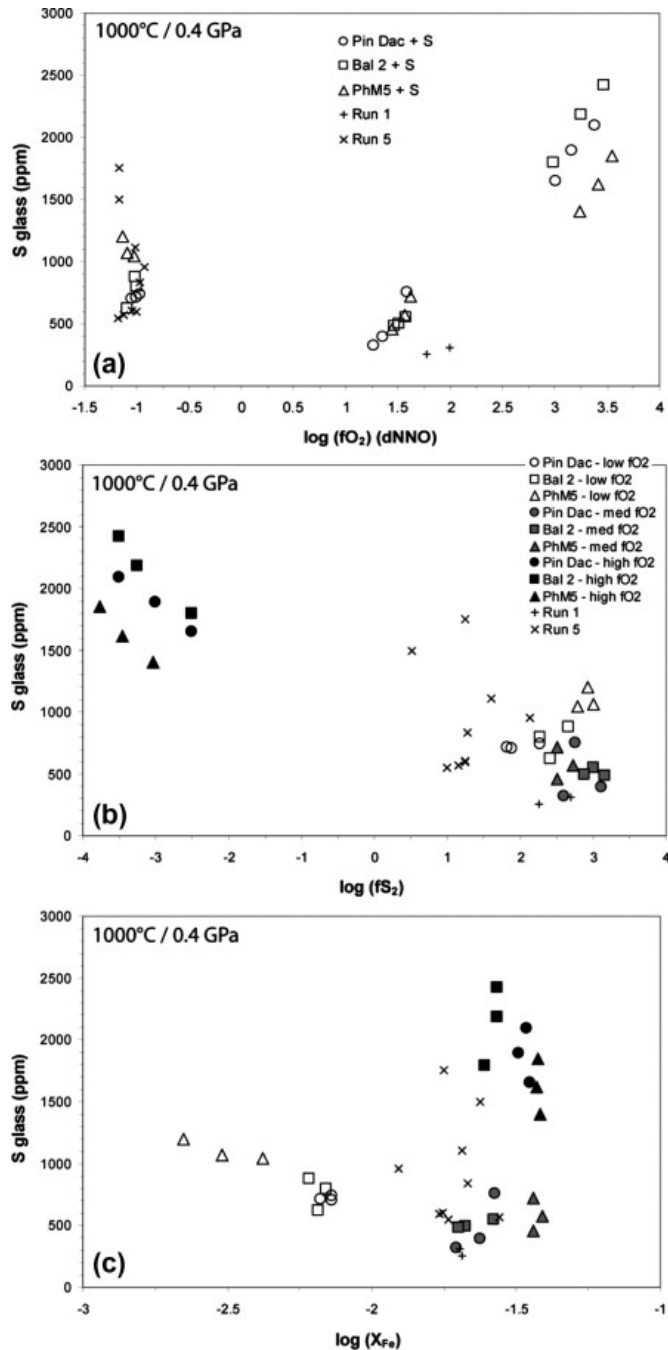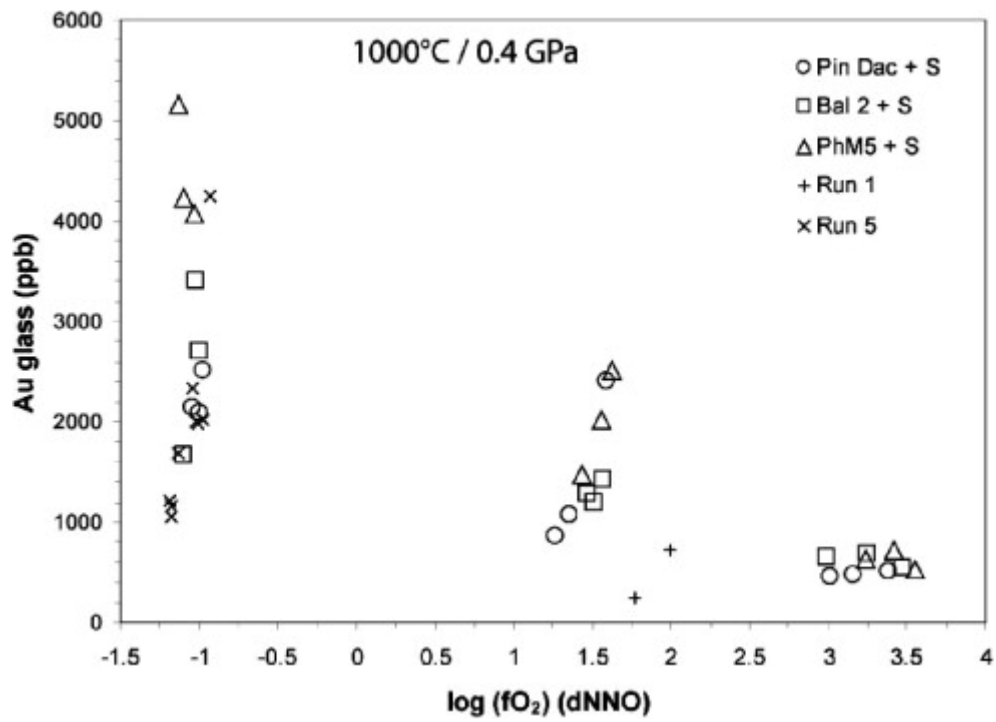

Fig. 4. Concentration of sulfur (in ppm) in experimental dacitic glasses at sulfide and sulfate saturation at 0.4 GPa and 1000 °C as a function of (a) log (fO_2) expressed relative to the Ni–NiO buffer (i.e., ΔNNO = 0), log (fS_2). (c) log (X_{Fe}). Each fO_2 range is shown with a different greyscale. The data from run 1 are distinguished (see text for details), as well as the data from run 5 ($fO_2 \sim$ NNO−1), whose quench was slower than intended.

Fig. 5. Concentration of gold (in ppb) in experimental glasses at sulfide and sulfate saturation at 0.4 GPa and 1000 °C as a function of log (fO_2), expressed relative to the Ni–NiO buffer (i.e., ΔNNO = 0).
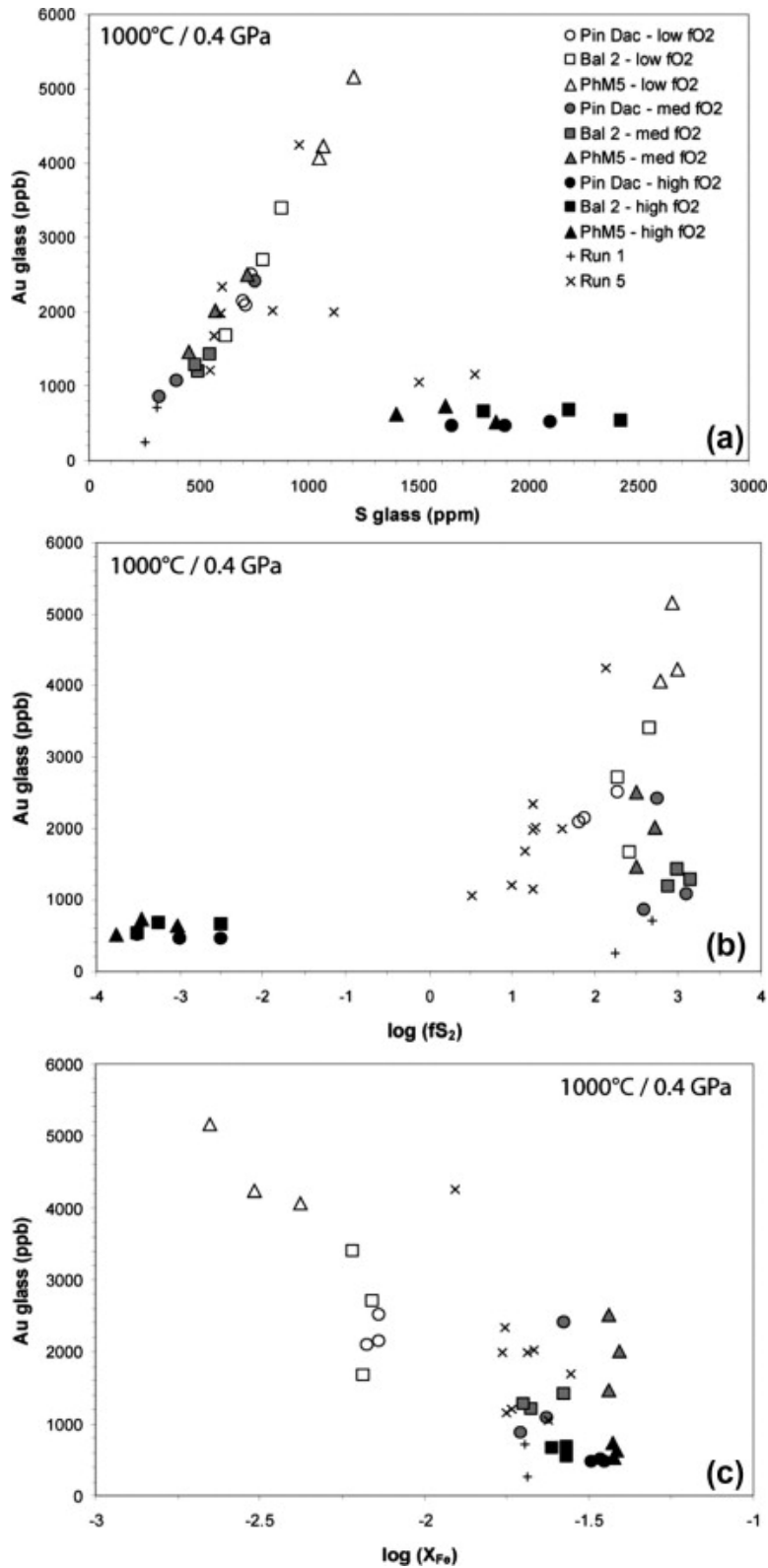
Fig. 6. Concentration of gold (in ppb) in experimental glasses at sulfide and sulfate saturation at 0.4 GPa and 1000 °C, (a) as a function of the glass sulfur content (in ppm); (b) as a function of log (fS_2); (c) as a function of log (X_{Fe}). Each fO_2 range is shown with a different greyscale.
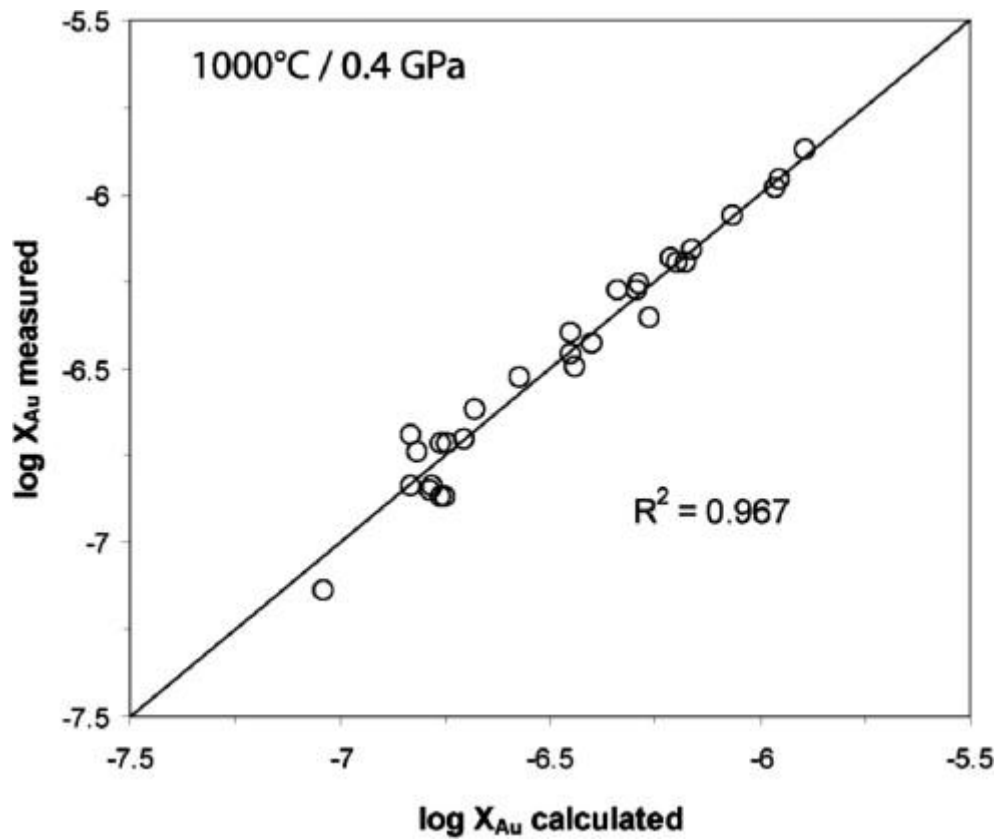
Fig. 7. Comparison between measured and modeled gold concentrations at 1000 °C and 0.4 GPa, expressed as logarithms of mole fractions in the melt. The whole dataset (except run 5, see text) has been considered in the gold dissolution model.
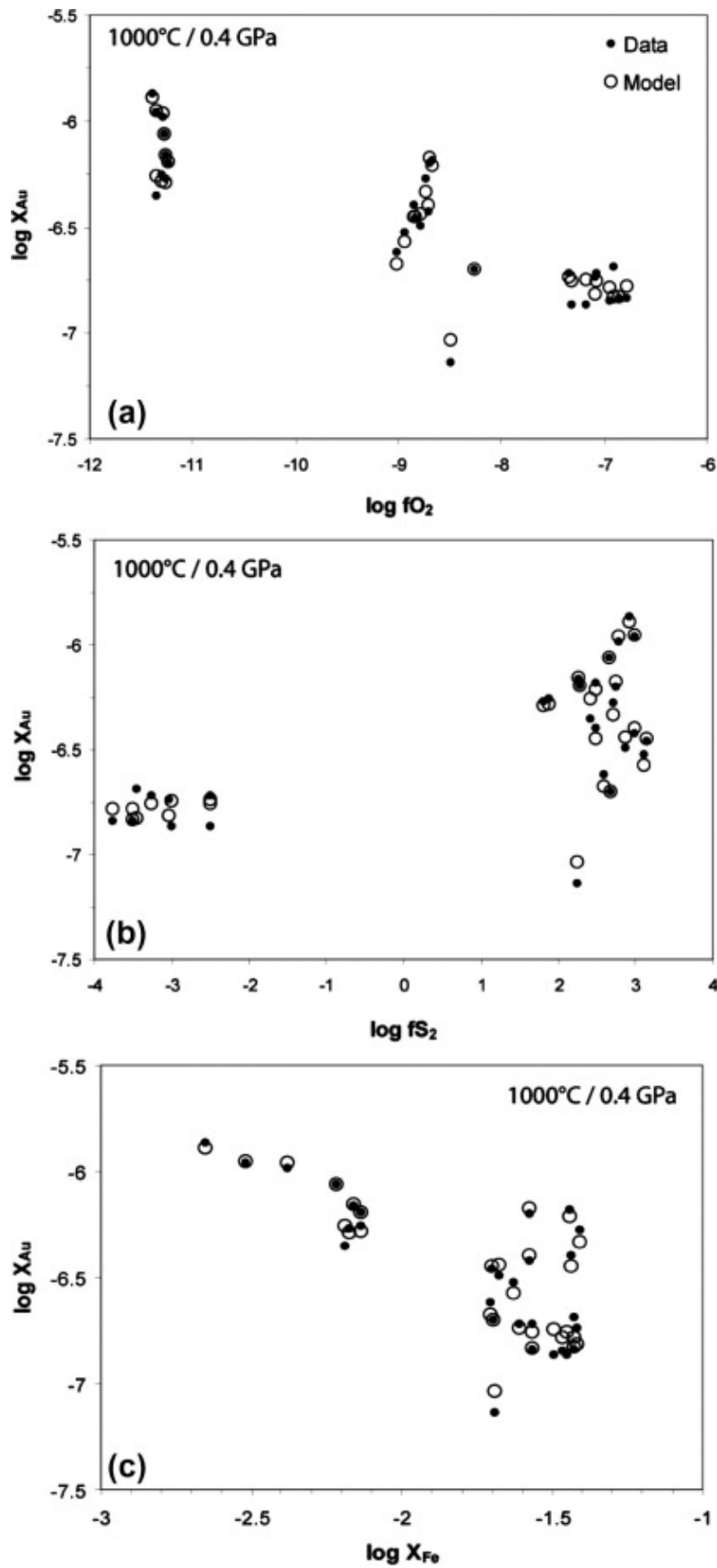
Fig. 8. Results of the Au solubility model shown as a function of (a) log (fO$_2$), (b) log (fS$_2$), (c) log (X_{Fe}). The experimental data are shown for comparison.
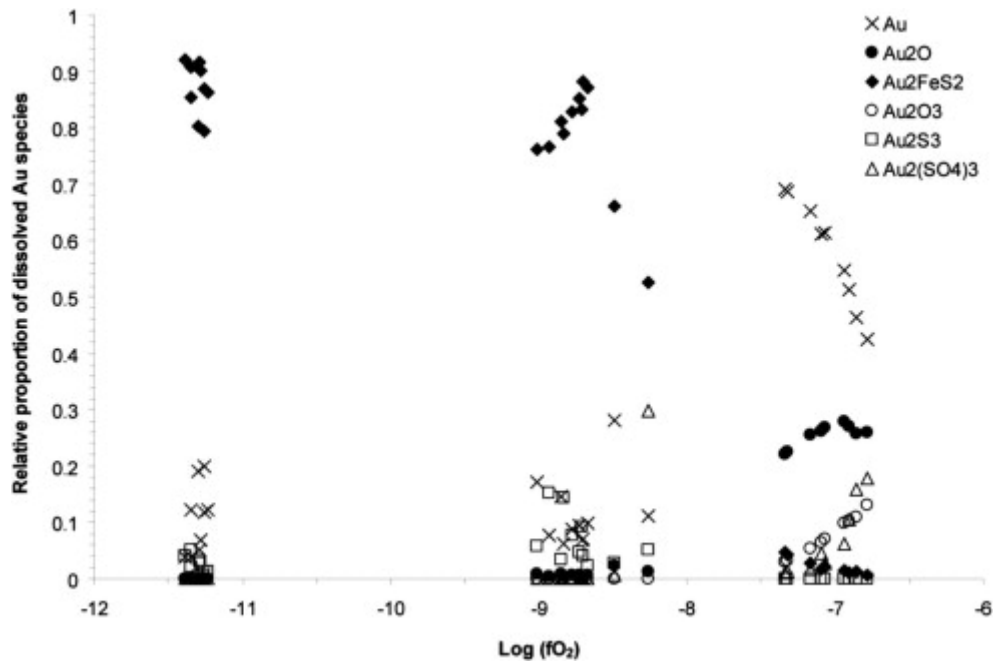
Fig. 9. Speciation diagram showing the relative proportions of gold species dissolved in hydrous dacitic melts as a function of log (fO_2), calculated from the Au solubility model. The black crosses are for Au species, the green symbols are for Au^{1+} species (i.e., Au_2O and Au_2FeS_2), and the red symbols are for Au^{3+} species (i.e., Au_2O_3, Au_2S_3, and $Au_2(SO_4)_3$), respectively. See Appendix A.3 and text for details.
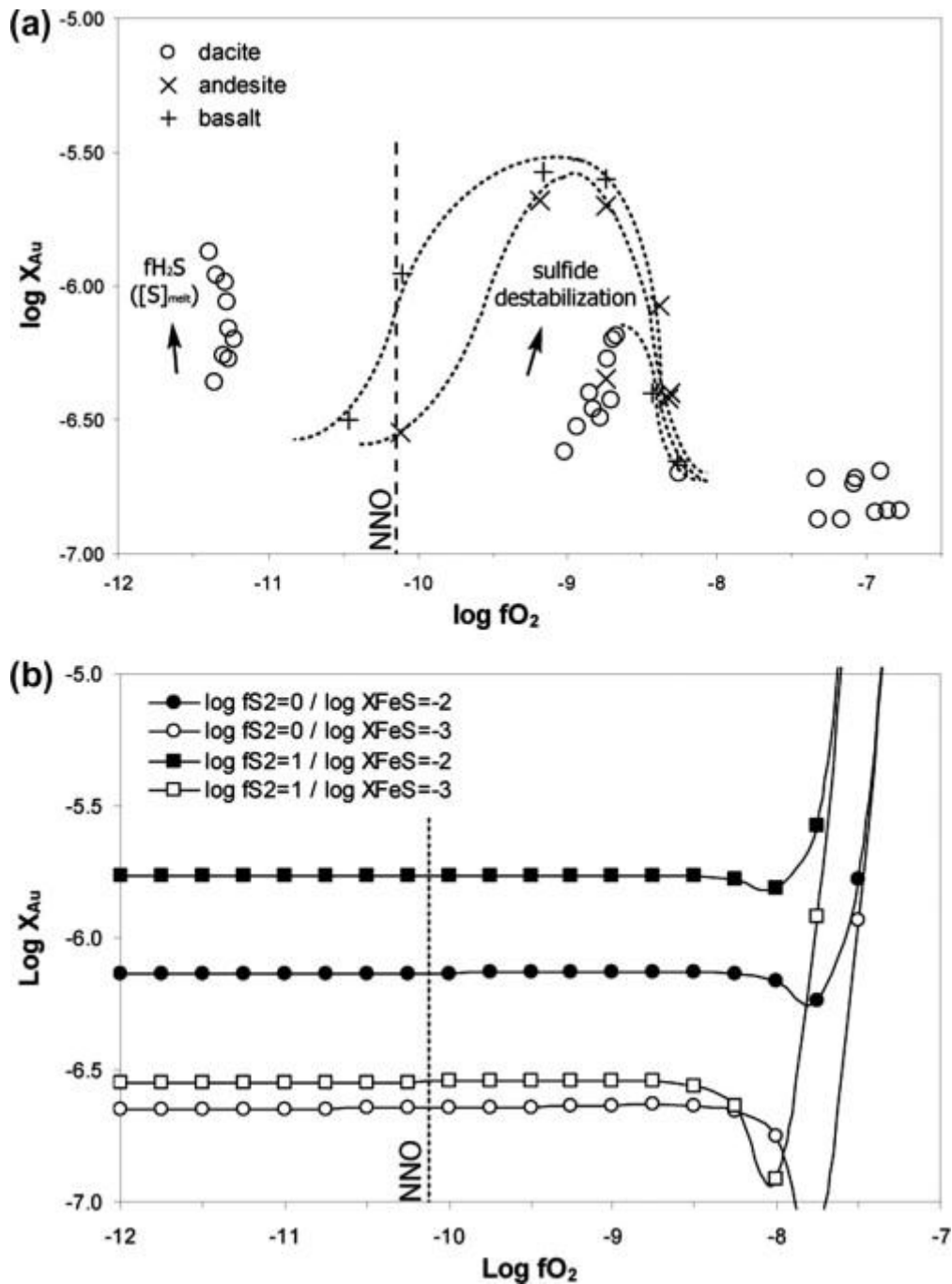
Fig. 10. (a) Evolution of the solubility of gold (in log (X_{Au})) in experimental glasses as a function of log ($f O_2$) for the whole dataset of the present study (except run 5; open circles) and the data of Botcharnikov et al. (2011) for basaltic (crosses and dashed line) and andesitic (tilted crosses and dashed line) melts at 0.2 GPa and 1050 °C. Note (1) the displacement of the maximum Au solubility under moderately oxidizing conditions towards higher $f O_2$ with increasing melt differentiation and (2) the region of elevated Au solubility in our dataset under reducing conditions (see text for discussion). (b) Theoretical Au solubility calculated as a function of log($f O_2$) for two different values of $f S_2$ and X_{FeS}, 0 or 1 and −2 or −3, respectively. The four dotted lines therefore represent a gold solubility baseline at constant $f S_2$ and X_{FeS} along the $f O_2$ range corresponding to sulfide saturation. Note the significant increase of Au solubility with increasing $f S_2$ and/or X_{FeS}. The hollow as well as the dramatic increase of Au solubility under oxidizing conditions are artefacts of the model due to too high $f S_2$ values.

Table S1.

	Species j	Charge i	Charge $i+1\ldots n$
	X_i Au (metal)	1	1
	X_i Au$_2$O	10^(0,5 log fO$_2$)	10^(0,5 log fO$_2$)
	X_i Au$_2$O$_3$	10^(1,5 log fO$_2$)	10^(1,5 log fO$_2$)
	X_i Au$_2$S	10^(0,5 log fS$_2$)	10^(0,5 log fS$_2$)
Matrix A_{ij} = abundances of gold species j dissolved in silicate melt in charge i	X_i Au$_2$S$_3$	10^(1,5 log fS$_2$)	10^(1,5 log fS$_2$)
	X_i Au$_2$SO$_4$	10^(2 log fO$_2$)·10^(0,5 log fS$_2$)	10^(2 log fO$_2$)·10^(0,5 log fS$_2$)
	X_i Au$_2$(SO$_4$)$_3$	10^(6 log fO$_2$)·10^(1,5 log fS$_2$)	10^(6 log fO$_2$)·10^(1,5 log fS$_2$)
	X_i Au$_2$FeS$_2$	10^(log X_{FeS})·10^(0,5 log fS$_2$)	10^(log X_{FeS})·10^(0,5 log fS$_2$)
	X_i AuFeS$_{2.5}$	10^(log X_{FeS})·10^(0,75 log fS$_2$)	10^(log X_{FeS})·10^(0,75 log fS$_2$)
log X_i Au calculated	Au total	log $\sum$ [(10^C_j)·X_{ij}]	log $\sum$ [(10^Cj)·$X_{i+1}\ldots n_j$]

Table S2.

Matrix $C = [((A_t \cdot A_{ij})-1) \cdot A_t] \cdot B = 10^{\wedge}C_j$

10^C_9	Au (metal)	1.886E−07
10^C_{10}	Au$_2$O	2.831E−04
10^C_{11}	Au$_2$O$_3$	8.678E+02
10^C_{12}	*Au$_2$S*	*−2.049E−08*
10^C$_{13}$	Au$_2$S$_3$	7.949E−12
10^C$_{14}$	*Au$_2$SO$_4$*	*−7.693E+08*
10^C$_{15}$	Au$_2$(SO$_4$)$_3$	1.654E+39
10^C$_{16}$	Au$_2$FeS$_2$	6.474E−05
10^C$_{17}$	*AuFeS$_{2.5}$*	*−8.033E−06*

Matrix of solutions 10^C_j. Lines *in italic* refer to gold species that are theoretically not present in the silicate melt; see text for explanations.